Pharmacologic hyperstabilisation of the HIV-1 capsid lattice induces capsid failure

K. M. Rifat Faysal[1], Nadine Renner[2,#], Chantal L. Márquez[1,#], Vaibhav B. Shah[1], Andrew J. Tuckwell[1], Michelle P. Christie[3], Michael W. Parker[3,4], Stuart G. Turville[5], Greg J. Towers[6], Leo James[2], David A. Jacques[1,*], Till Böcking[1,*]

1. EMBL Australia Node in Single Molecule Science, School of Biomedical Sciences, UNSW Sydney, NSW 2052, Australia

2. MRC Laboratory of Molecular Biology, Cambridge, United Kingdom

3. Department of Biochemistry and Pharmacology, Bio21 Molecular Science and Biotechnology Institute, University of Melbourne, Victoria 3010, Australia

4. Structural Biology Unit, St. Vincent's Institute of Medical Research, Victoria, Australia

5. The Kirby Institute, UNSW Sydney, NSW 2052, Australia

6. Division of Infection and Immunity, University College London, WC1E 6BT London, United Kingdom

[#]equal contribution
*Corresponding authors: David Jacques (d.jacques@unsw.edu.au); Till Böcking (till.boecking@unsw.edu.au)

Abstract

The HIV-1 capsid has emerged as a tractable target for antiretroviral therapy. Lenacapavir, developed by Gilead Sciences, is the first capsid-targeting drug approved for medical use. Here we investigate the effect of Lenacapavir on HIV capsid stability and uncoating. We employ a single particle approach that simultaneously measures capsid content release and lattice persistence. We demonstrate that Lenacapavir's potent antiviral activity is predominantly due to lethal hyperstabilisation of the capsid lattice and resultant loss of compartmentalisation. This study highlights that disrupting capsid metastability is a powerful strategy for the development of novel antivirals.

Introduction

The cytoplasm is a hostile environment for HIV, as the reverse transcribed cDNA genome is a target for innate immune sensors which if activated unleash a potent interferon response that can suppress replication (Alvarez et al., 2022; Lahaye et al., 2013; Rasaiyaah et al., 2013). For a productive infection to occur, the reverse transcribing genome must be trafficked through the cytoplasm, enter the nucleus and integrate into the preferred sites in the host chromatin, all while evading detection by the host cell. The viral capsid facilitates these early steps in the replication cycle by encapsulating the genome and associated viral enzymes. In doing so it protects the genome from being sensed and destroyed by nucleases, prevents loss of viral enzymes from the reverse transcription complex, and forms the interface through which all cytoplasmic, and many nuclear, host-virus interactions occur.

The conical capsid shell is comprised of ~1500 copies of the capsid protein (CA), which spontaneously assemble into a lattice. This lattice consists of mostly hexamers and exactly 12 pentamers to form a closed fullerene cone (Ganser et al., 1999; Pornillos et al., 2011). While the capsid must be stable enough to transit the cytoplasmic compartment without exposing the genome, it must also be able to release the reverse transcribed cDNA at the appropriate time and in the appropriate location in the nucleus. This process is called capsid uncoating and its regulation and mechanism is poorly understood. Recently, we demonstrated that uncoating proceeds through two discrete steps *in vitro*: capsids opening, in which the integrity of the cone is compromised and encapsidated proteins are released; and catastrophic disassembly of the lattice by release of CA (Márquez et al., 2018). We have also shown that recruitment of cellular cofactors or binding of pharmacological agents to the capsid can greatly alter both processes.

To engage with host cofactors, the mature HIV capsid utilises at least three cytoplasmic-facing surfaces (Temple et al., 2020). One of these is the central pore, which is formed by a ring of positively charged arginine residues at the six-fold symmetry axis in CA hexamers and at the five-fold axis in pentamers (Jacques et al., 2016). It serves to recruit nucleotides required for reverse transcription and as a binding site for inositol hexakisphosphate (IP6), a metabolite present at concentrations of ~40–50 μM in human cells (Bunce et al., 1993; Letcher et al., 2008; Veiga et al., 2006). IP6 is specifically packaged into immature virions during assembly in producer cells, leading to a ≥10–fold enrichment, and its interaction with the central hexamer pore is essential for the assembly and stability of the capsid (Dick et al., 2018; Mallery et al., 2018; Obr et al., 2021; Sowd and Aiken, 2021). The central pore has also been implicated in the capsid's interaction with microtubule-based motor proteins (Huang et al., 2019).

Another important interface is the cyclophilin binding loop. As its name suggests, this largely unstructured loop protrudes from the capsid surface to recruit cyclophilin A (CypA). This interaction is mediated by a conserved glycine-proline motif (G89-P90) that inserts into the CypA active site. The implications of this interaction are still to be fully understood, but are thought to include viral evasion of innate host defences (Kim et al., 2019; Miles et al., 2020; Rasaiyaah et al., 2013; Towers et al., 2003). Importantly, we have previously shown that this interaction can be exploited *in vitro* to ‘paint’ the capsid (Márquez et al., 2018). By using a fluorescently labelled CypA, we found that it is possible to detect, quantify, and monitor disassembly of the CA lattice in permeabilised virions by total internal reflection fluorescence (TIRF) microscopy without significantly influencing the capsid opening process.

The third host-interaction surface, the FG-binding site, is a hydrophobic pocket in the CA N-terminal domain situated near the intra-hexameric junction between CA molecules (Figure 1). This site serves as the binding interface for several host factors, including the cytoplasmic protein Sec24C (Rebensburg et al., 2021), the nuclear pore complex component NUP153 (Matreyek et al., 2013), and the nuclear protein CPSF6 (Bhattacharya et al., 2014; Price et al., 2014), which are crucial for nuclear entry and correct integration site targeting (Bejarano et al., 2019; Saito et al., 2016; Schaller et al., 2011). Each of these proteins interacts with the capsid via a phenylalanine-glycine (FG) motif. Additionally, several generations of antiviral compounds also target this site by effectively mimicking the FG-motif (Price et al., 2014). Interestingly, the potency and mechanism of action of these agents varies, despite their shared binding site.

Compounds that target the FG-binding pocket include BI-2 (Lamorte et al., 2013), PF74 (Blair et al., 2010), and lenacapavir (LEN, GS-6207) (Link et al., 2020). BI-2 has a relatively small binding footprint on the CA N-terminal domain, barely extending beyond the FG-binding pocket (Figure 1A). This limited interaction is reflected in the relatively weak K_D (1.2 μM) and half maximal inhibitory concentration (IC50) (3 μM) during the early stage of infection (Price et al., 2014). PF74, on the other hand, extends its interaction beyond the FG-binding pocket to make additional contacts with a neighbouring CA molecule (Figure 1B). These bridging contacts are thought to be responsible for PF74's 10-fold tighter K_D (120 nM) and IC50 (relative to BI-2). Both BI-2 and PF74 have been shown to compete with host cofactors (Sec24C, Nup153, and CPSF6) (Fricke et al., 2014; Matreyek et al., 2013; Peng et al., 2014; Price et al., 2014; Rebensburg et al., 2021), but have also been suggested to destabilise the capsid directly (Bhattacharya et al., 2014; Fricke et al., 2014; Shi et al., 2011), which interferes with reverse transcription (Jennings et al., 2020; Mallery et al., 2018; Sowd et al., 2021). In contrast to BI-2 and PF74, which have found use exclusively in the laboratory, LEN is a first-in-class HIV-1 capsid inhibitor currently in clinical trials (Dvory-Sobol et al., 2022; Link et al., 2020). Structurally, LEN makes extensive contacts across two neighbouring CA monomers (Figure 1C), allowing for a very high-affinity interaction (K_D = 215 pM). It interferes with early and late phases of the HIV-1 replication cycle at low and mid pM concentrations, respectively, making it orders of magnitude more potent than PF74 and BI-2 (Bester et al., 2020; Link et al., 2020). Successive post-entry steps differ in their sensitivity to the drug (Bester et al., 2020; Link et al., 2020), whereby integration of HIV-1 DNA into host chromatin is inhibited most potently (<500 pM), followed by nuclear import and reverse transcription, which is inhibited at high pM (Sowd et al., 2021) to low nM LEN (Bester et al., 2020). Remarkably, imaging studies (Bester et al., 2020) and biochemical assays (Selyutina et al., 2022) showed that LEN increased the number of viral cores in the cytoplasm in a dose-dependent manner. Thus, the drug apparently exhibited contrasting inhibitory effects at higher concentrations: inhibition of reverse transcription and stabilization of viral cores.

Here we have used our single-molecule fluorescence imaging assay with a dual read-out strategy to show that LEN compromises capsid integrity while preventing lattice disintegration at substoichiometric levels of binding, thus providing a rationale for the attenuated reverse transcription and capsid stabilization previously observed at nanomolar concentrations of the drug. PF74 induces the same effects but with less potency, while BI-2 leads to rapid capsid breakage but does not prevent disintegration. Conversely, a peptide from CPSF6 has modest capsid-breaking capacity but strongly promotes lattice stability, suggesting that FG pocket binders differentially affect these steps of the uncoating process. We also show that LEN drives the formation of aberrant CA structures, which cannot be

rescued by IP6. Altogether, our data suggest that LEN promotes CA assembly and stability at the cost of intact fully closed capsids.

Results

Single-virion analysis of intrinsic capsid stability and uncoating.

We used a single-molecule fluorescence imaging assay to measure the intrinsic capsid stability and uncoating kinetics at the level of individual viral particles (Márquez et al., 2018) and then measured the effect of LEN treatment on these processes. As shown schematically in Figure 2A, we used pore-forming proteins to permeabilise GFP-loaded HIV particles immobilised at the bottom surface of a microfluidic channel device. Using TIRF microscopy, we then detected the stepwise loss of the GFP signal for each virion appearing as a diffraction-limited spot in the field of view. Upon membrane permeabilization, virions with an incomplete or defective capsid lost their entire GFP signal in a single step (Figure 2B, "leaky"). In contrast, virions containing an intact capsid retained the pool of GFP inside the capsid (~10-20% of the total fluorescence). This residual GFP signal was either constant when the capsid remained intact throughout the experiment (Figure 2B, "closed") or lost in a second step upon spontaneous loss of capsid integrity (Figure 2B, "opening"), whereby the lifetime of each opening capsid was given by the time difference between the two GFP release steps.

To quantify the capsid uncoating kinetics across the typically several hundred virions per field of view in an unbiased fashion, we used step-fitting to measure the lifetime of each capsid and classify particles according to the GFP release profiles defined above. The distribution of capsid lifetimes (survival curve) for untreated virions (Figure 2D, no drug) showed the typical multiphasic decay profile reflective of different capsid stability types. The corresponding classification showed that more than half of virions contained improperly assembled (leaky) capsids, about a third of virions released GFP from the capsid (short- and long-lived opening) while the remainder retained GFP (closed) until the end of the 30 min experiment (Figure 2E).

As a complementary measurement, we used AF568-labelled CypA as a "paint" that binds transiently to the outside of the capsid, rapidly reaching a dynamic equilibrium, whereby the AF568-CypA intensity is proportional to the number of CA subunits in the lattice. Importantly, AF658-CypA was used at concentrations (0.5–1 μM) where fewer than 4% of the available cyclophilin loops are occupied, and we have previously shown that uncoating kinetics are not affected under these conditions (Márquez et al., 2018). Single-particle analysis showed that the AF568-CypA signal remained constant while the capsid was intact (Figure 2B, "closed") but decayed to background levels after the capsid opened (Figure 2B, "leaky" and "opening"). Analysis of all leaky and opening traces aligned to the time of GFP release (represented as CypA paint heatmaps, Figure 2−Figure Supplement 2A) showed that the median CypA signal decayed with a half-life of less than 1 minute. This rapid decay is consistent with a failure cascade that propagates across the whole capsid resulting in complete lattice disassembly. Taken together, our single-particle analysis shows that GFP release pinpoints the time the first defect appears in the capsid while the CypA paint signal provides an indirect read-out for the disassembly kinetics of the CA lattice thereafter.

LEN induces capsid opening but prevents loss of CA from the lattice of open capsids.

In the next set of experiments, we focused on the effect of LEN on the intrinsic capsid stability without capsid-binding cofactors; the interplay between LEN and the host cofactor IP6, which is essential for maintaining capsid stability in cells, is described in later sections. To measure the maximum effect of LEN on capsid uncoating, we added the drug at the beginning of the experiment at a concentration (500 nM) that leads to rapid near saturation

occupancy (99.96%) of FG binding sites. Uncoating traces recorded of single virions in the presence of 500 nM LEN (Figure 2C) revealed two fundamental differences to the single-particle profiles described above. First, LEN treatment caused earlier release of the encapsidated GFP (Figure 2C, "opening"), resulting in a faster decaying survival curve (Figure 2D, light green line) and a concomitant 3-fold decrease in the fraction of closed capsids at the end of the experiment (Figure 2E). Second, the AF568-CypA signal of capsids that were defective to begin with (Figure 2C, "leaky") or started to uncoat (Figure 2C, "opening") remained constant. This striking stabilisation effect was also clear in the heatmaps of leaky and opening capsids (Figure 2–Figure Supplement 1B). Since the CypA paint traces of leaky and opening capsids showed the same characteristics, we combined these classes in subsequent analysis. The combined CypA paint heatmaps for untreated virions (rapid signal decay) and LEN-treated virions (constant signal) are shown in Figure 3C (see panels for 0 nM and 500 nM, respectively). Together, the GFP release and CypA paint analysis in the presence of 500 nM LEN suggest that binding of LEN induces rupture of capsids (leading to early GFP release) but prevents the loss of CA subunits from defective or ruptured capsids (stable CypA paint signal).

To further quantify these apparently opposing effects on capsid integrity and CA lattice stability, we injected LEN at concentrations ranging from 0.5–500 nM into the flow channel at the beginning of the experiment and measured GFP release and CypA paint traces for hundreds of capsids at each condition (Figure 3). Control uncoating experiments recorded without LEN resulted in the typical survival kinetics (Figure 3A, 0 nM LEN) with capsid half-lives of 1–2 minutes (short-lived) or ~16 minutes (long-lived) reflecting subsets of virions with less or more stable capsids, respectively (Figure 3–figure supplement 1). Classification based on GFP release traces showed on average 55% leaky, 35% opening (comprising 12% short-lived and 23% long-lived capsids) and 10% closed capsids at the end of the experiment (Figure 3B, 0 nM LEN). However, treatment with LEN resulted in a 2-fold (5 nM) or 3-fold (≥50 nM) decrease in the proportion of capsids that remained closed throughout the experiment (30 min) with a concomitant increase primarily in the fraction of leaky and short-lived capsids (Figure 3B). This decrease in capsid stability was also apparent in the survival curves (Figure 3A), showing a pronounced concentration-dependent increase in capsid opening kinetics with an intermediate effect at 5 nM and the maximal effect at ≥50 nM LEN. Analysis of the CypA paint signal of particles with leaky or opening capsids (Figure 3C) showed that the CA lattice disassembled within ~1 minute of the appearance of the first defect at LEN concentrations ≤5 nM. In contrast, LEN at concentrations of ≥50 nM prevented disassembly of leaky and opening capsids, as evidenced by the stable CypA paint signal (Figure 3C), which persisted for at least 5 h (500 nM) after complete loss of GFP (Figure 3D). In summary, LEN dose-dependently increased the proportion of open capsids but increased the stability of their lattices. The dose-dependence observed here differs from previous in vitro uncoating measurements showing (partial) capsid lattice stabilisation down to 0.05 nM LEN; in those experiments 50–65% of cores stained with the irreversibly bound tetrameric probe CypA-dsRed remained detectable after 30 min of incubation (Bester et al., 2020). Nevertheless, our observations of open but highly stabilised capsids is consistent with the LEN dose-dependent increase in the number of viral cores detected in the cytoplasm of infected cells (Bester et al., 2020; Selyutina et al., 2022).

To relate the capsid-altering effects of the drug to the occupancy of FG binding sites on the CA lattice, we used published association and dissociation rate constants for LEN (Link et al., 2020) to calculate the drug binding curves at the concentrations used in the experiments above (shown as bold beige lines for each concentration in Figure 3A). Notably, the time

required for binding to approach equilibrium ranges is >18 hours at 0.5 nM, ~2.5 hours at 5 nM, ~15 minutes at 50 nM and ~2 minutes at 500 nM. Under the conditions used in the single-particle uncoating assay, the capsid is exposed to the membrane-permeable drug for ~2 minutes before the pore forming protein permeabilises the viral membrane. Thus, we first calculated the occupancy at this time point to estimate the threshold required to stabilise defective capsids. Unsurprisingly, the low occupancy at 0.5 nM and 5 nM LEN (calculated to be 0.4% and 4%, respectively) was insufficient for lattice stabilisation. In contrast, 50 nM LEN, which should occupy 32% of sites, was sufficient to prevent CA lattice disassembly.

Next, we similarly estimated the threshold at which LEN was able to induce capsid breakage. At 0.5 nM, the calculated occupancy remains too low (<6%) throughout the experiment and uncoating kinetics were unaffected. In the presence of 5 nM LEN, the calculated occupancy is ~20% over the first 10 minutes after membrane permeabilisation, during which an intermediate effect on capsid opening was observed. Maximum capsid-breaking activity was observed at 50 nM LEN, whereby most capsid rupture during the first 5 minutes with the calculated occupancy reaching ~70–80%. Based on these considerations, we estimate that structural effects are already observed when fewer than half of the available binding sites are occupied, possibly requiring an average occupancy as low as 1 LEN molecule per hexamer to accelerate capsid opening and 2 LEN molecules per hexamer to slow the release of CA subunits from the lattice.

IP6 raises the threshold of drug binding required for LEN to break the capsid.

We have previously shown that the cellular cofactor IP6 stabilises capsids and delays capsid opening *in vitro,* hence increasing the half-life of the closed capsid to ~10 hours when added at a concentration of 100 μM (Mallery et al., 2018). Given IP6 is present in cells (typically 40–50 μM) and therefore expected to impact the effects of LEN *in vivo,* we asked if IP6 could prevent LEN-induced rupture of the capsid. As before, addition of IP6 (100 μM) to the solution strongly stabilised capsids in permeabilised virions, leading to reduced capsid opening kinetics (Figure 4A, 0 nM LEN/+IP6) and a ~3-fold increase in the fraction of closed capsids at the end of the experiment (Figure 4B, 0 nM LEN/+IP6). Next, we tested the effect of adding 100 μM IP6 in combination with LEN at concentrations above the threshold required to damage the integrity of the capsid (≥5 nM LEN). IP6 partially counteracted the capsid-breaking effect when <40% of FG sites are occupied (5 nM LEN), but even at this concentration the drug increased capsid opening kinetics relative to control with IP6 only (Figure 4A, compare 0 nM LEN/+IP6 and 5 nM LEN/+IP6). At high LEN concentrations (≥50 nM), the survival curves measured in the presence and absence of IP6 were essentially the same, showing that IP6 was no longer able to counteract the premature rupture of the capsid induced by the drug (Figure 4A, 50 nM and 500 nM). This acceleration in capsid opening (regardless of whether IP6 was present) led to a 10-fold reduction in the fraction of closed capsids to 3% at the end of the experiment compared to the control with IP6 only (Figure 4B, compare 0 nM LEN/+IP6 with 50 nM LEN/+IP6 or 500 nM LEN/+IP6). We conclude that IP6-stabilised capsids require a higher drug occupancy (>50% of sites) than in the absence of IP6 for defects to manifest. The ability of IP6 to counteract LEN-induced damage to the capsid has also been proposed based on observations by others that LEN more potently inhibits reverse transcription *in vitro* and in cells when IP6 levels are low (Sowd et al., 2021).

Finally, we analysed the CypA paint data from the above experiments to determine if IP6 could act in conjunction with LEN to stabilise the CA lattice when the capsid had opened. As observed for other polyanions binding at the R18 ring at the centre of the CA hexamer

(Márquez et al., 2018), IP6 slows but does not prevent the catastrophic collapse of the CA lattice once the first capsid defect has appeared (Figure 4–Figure Supplement 1). CA lattice dissociation of leaky and opening capsids is also slower but not completely inhibited when IP6 is added to 5 nM LEN (<10% occupancy of FG sites at the time of membrane permeabilization) (Figure 4–Figure Supplement 2A and B). At 50 nM LEN (>30% occupancy of FG sites), the CypA paint signal remains constant in the presence and absence of IP6 (Figure 4–Figure Supplement 2C and D), such that differences in stability during the time frame of the experiment are difficult to ascertain. Overall, these data suggest that IP6 further stabilises LEN-stabilised CA lattices but not to the extent where it can prevent CA release from lattices at low LEN occupancy.

Slow LEN binding kinetics delay the structural drug effects at low concentrations.

To verify that LEN binding kinetics affect the structural effects on capsid, we preincubated virions with 5 nM LEN for 4 h, during which 95% of sites are occupied. Analysis of GFP release traces showed that preincubation increased the fraction of leaky capsids from 60% to 80% (Figure 5A and B) concomitant with the loss of short-lived opening capsids, suggesting that this comparatively less stable subset is more susceptible to LEN-induced rupture. CypA paint analysis showed that CA lattice disassembly was inhibited with, but not without, preincubation (Figure 5C). These observations suggest that the full extent of the capsid-altering effects is observed after binding occupancy reaches the requisite threshold level. The increase in the fraction of leaky capsids after preincubation (exceeding the fraction of leaky capsids observed at 500 nM without preincubation, Figure 3B) further suggests that drug-induced capsid rupture manifests over time and that rupture, or build-up of the strain required for rupture, can already occur before release of the capsid from the virion.

Next, we tested whether preincubation of virions with LEN for 48 h would result in higher potency of the drug in Jurkat cells infected with VSV-G pseudotyped HIV encoding GFP as a reporter. We chose 48 h because this time is required for binding at the reported 50% inhibitory concentration (IC50) of ~0.05–0.1 nM to reach near equilibrium (Figure 5–Figure Supplement 1). Similar to the capsid-targeting drug PF74 (Price et al., 2014; Saito et al., 2016), the dose-response curves of LEN showed a biphasic inhibition profile, whereby the first phase (~0.1 nM) reduced infection to about 10% before a second inhibitory mechanism operating in the low nM range reduced infection levels to less than 1%. Preincubation had little effect on inhibition during the first phase and resulted in an only 1.3-fold reduction in IC50 (Figure 5D and E). This observation suggests that without preincubation infection was blocked sufficiently late post entry such that the drug had sufficient time to reach the requisite occupancy threshold. The IC50 measured after preincubation (0.093±0.008 nM) allowed us to calculate that the first inhibitory phase required LEN to bind to ~30% of sites (assuming that the LEN concentration in the cell is the same as in that added to the culture medium). To reach this level of binding (30%) at the IC50 measured without preincubation (0.125±0.013 nM) would require 20 hours (see corresponding occupancy curve in Figure 5D). This analysis suggests that the low concentration block to infection occurs at a step after nuclear entry.

In contrast to the modest effect at low LEN concentrations, preincubation reduced infection 2–3-fold at concentrations ≥0.256 nM (i.e., during the second inhibitory phase), whereby the IC95 was 0.5 nM and 1 nM with and without preincubation, respectively (Figure 5D). To estimate the time at which the second block occurs, we first calculated that ~70% of sites were occupied at equilibrium at 0.5 nM LEN (i.e., at the IC95 with preincubation). This level is also reached 7 hours after addition of 1 nM LEN (IC95 without preincubation). Overall, we

conclude that LEN inhibits a late post-entry step when binding to ~30% of sites (reached at ~0.1 nM without preincubation), but this block is insufficient to reduce infection below a level of ~10%. At ≥70% occupancy of sites on the CA lattice, LEN additionally blocks infection at a step that occurs 7 hours post infection, ultimately reducing infection to levels below 1%.

Next, we determined the dose-dependent effect of LEN on reverse transcription using qPCR with primers amplifying total viral DNA (Figure 5F). The IC50 for reverse transcription in Jurkat cells was 1.08 nM LEN without preincubation, consistent with the dose-response in CEM cells (IC50 = 0.68 nM) (Sowd et al., 2021). This value dropped to 0.59 nM when virions were preincubated for 48 h with LEN prior to infection. Inspection of the occupancy curves (Figure 5F) revealed that half-maximal inhibition of reverse transcription required an occupancy of ~70% and occurred at ~7 h after cell entry, coinciding with 95% inhibition of infection. Overall, this analysis showed that reverse transcription can no longer proceed as a result of the second inhibition mechanism of LEN.

LEN and IP6 synergise to promote CA assembly but compete to bias the assembly pathway towards tube (LEN) versus cone (IP6) formation.

Since both IP6 (Dick et al., 2018; Renner et al., 2021) and LEN (Bester et al., 2020; Link et al., 2020) promote CA assembly and lattice stability *in vitro*, we tested how the combination of these molecules affects CA assembly in low salt conditions. We monitored the assembly kinetics of recombinant CA by measuring the absorbance at 350 nm and collected samples at the end of each experiment for analysis by negative stain electron microscopy (Figure 6). First, we varied the concentration of IP6 and observed that CA (75 μM) assembled with similar kinetics in the presence of 100 μM or 150 μM IP6 but did not assemble at lower IP6 concentrations (Figure 6A, left). As expected, negative stain EM images of assembly products formed with only IP6 showed primarily conical shapes with dimensions, similar to those observed for native HIV capsids (Figure 6A, right). When we repeated this titration in the presence of 50 μM LEN (substochiometric relative to CA), we observed CA assembly across the entire concentration range (10–150 μM IP6), with IP6 accelerating assembly kinetics and yields in a concentration-dependent manner (Figure 6B). Strikingly, LEN in the presence of low IP6 promoted formation of CA tubes (often closed at their ends) with lengths of >500 nm, whereby increasing IP6 concentrations biased assembly increasingly towards shorter tubes and conical shapes. Next, we varied the concentration of LEN in the presence of 200 μM IP6. Addition of 1–50 μM LEN increased CA assembly efficiency in a concentration-dependent manner above the level observed for IP6 only (Figure 6C, left). Notably, the highest LEN concentration (50 μM) did not promote CA (75 μM) assembly without IP6 in low salt conditions (Figure 6B, left). Negative stain EM images confirmed cone formation in the presence 200 μM IP6 and showed that addition of drug led to the formation of aberrant and broken structures in a concentration-dependent manner (Figure 6C, right). We conclude that LEN is insufficient to promote CA assembly by itself in low salt conditions but synergises with IP6 to increase assembly kinetics and yields. Importantly, IP6 promotes cone assembly, whereas LEN biases assembly toward tube formation such that closed tubes form in the presence of high drug and sufficiently low IP6. When both molecules are present at high concentrations, where neither molecule can dominate the assembly pathway, assembly proceeds in an aberrant fashion yielding heterogeneous structures. Taken together these observations show that IP6 and LEN synergise to promote assembly but preferentially stabilise different CA lattice structures. Since IP6 is enriched in HIV particles (reaching concentrations of ~500 μM (Mallery et al., 2018)), this drug-cofactor synergy driving aberrant assembly is likely to play out during capsid assembly in virions

produced in the presence of drug, consistent with the observation that virions produced in the presence of LEN (Link et al., 2020) or the closely related compound GS-CA1 (Yant et al., 2019) contain improperly shaped capsids.

LEN promotes CA overassembly inside mature virions.

As the single-particle TIRF analysis suggested that LEN alters capsid properties inside the intact virion, we used cryo-electron tomography (cryoET) to image purified virions that were either left untreated or treated with 700 nM LEN for 30 minutes (Figure 7), conditions that are expected to essentially saturate FG binding sites on the capsid. We carried out 3-dimensional reconstructions on 139 untreated and 96 drug-treated virions and assigned the tomograms to one of five categories according to maturation state and appearance of the capsid (Figure 7A) as in previous work (Fontana et al., 2016; Mallery et al., 2021; Mattei et al., 2014; Renner et al., 2021). As expected, the virion preparation contained a small fraction of particles with immature lattice (<10%) irrespective of drug treatment. Most untreated particles contained mature capsids with a conical or tubular morphology (74%) while a smaller fraction contained mature capsids with an irregular shape (17%). These categories were largely unaffected by incubation with LEN but showed a small shift from particles with conical/tubular capsid (64%) to particles with irregular capsids (25%). While the tomograms of virions with LEN did not reveal obvious capsid defects (such as large holes or capsid breakage), we frequently observed additional lattices next to the main capsid. To quantify the different types of additional structure, we further divided particles with a conical/tubular capsid into subclasses depending on whether they contained an open CA lattice or additional capsids and/or whether a second CA layer had formed around the capsid (Figure 7B). As expected, untreated virions contained mostly single capsids comprised of a single CA layer (74%) and a minority contained additional open (13%) or closed (7%) lattices. Double layered capsids were infrequent (6%). In stark contrast, we observed that almost all drug-treated virions contained additional CA structures (61%) and/or appeared with a double layered capsid (45%) while canonical capsids (single closed structure comprised of a single CA layer) were infrequent (<4%). These observations suggest that LEN induces assembly of the pool of free CA that is otherwise not incorporated into the capsid. To corroborate this overassembly phenotype and obtain an estimate of its kinetics, we used our TIRF assay to obtain the intensity of the CypA paint signal as a measure of CA lattice size. This analysis showed an average 1.7–1.8-fold increase of the CypA paint signal in virions treated with 500 nM LEN relative to untreated control (Figure 7C and Figure 7–Figure Supplement 1), consistent with the presence of a larger overall CA lattice surface area contained within the permeabilised membrane. This CypA paint signal increase was already observed after short incubation (2 minutes) and did not increase further after longer incubation (30 minutes) suggesting that CA overassembly induced at high drug concentrations inside mature virions is rapid.

PF74 but not BI-2 slows CA lattice disassembly after capsid rupture.

We have shown before using single-molecule TIRF uncoating assays that PF74, an HIV inhibitor that binds to the same site as LEN, strongly accelerates capsid opening and stabilises the lattice of the capsid thereafter (Márquez et al., 2018). The concentration (10 μM) used in those experiments is 40–80-fold above the K_D determined for the interaction with CA hexamers (between 0.12 μM (Price et al., 2014) to 0.26 μM (Bhattacharya et al., 2014)), such that 97–99% of binding sites of the capsid are predicted to be occupied with a drug molecule. PF74 is an important tool to study HIV capsid-associated processes but has been described to either promote capsid uncoating (Santos et al., 2016; Selyutina et al., 2022; Shi et al., 2011) or to stabilise capsids (Rankovic et al., 2018) or to have no effect on capsid

integrity (Hulme et al., 2015). To resolve this ambiguity and further characterise the ability of PF74 to stabilise CA lattices, we carried out CypA paint experiments in the presence of 0.1–10 μM PF74 (Figure 8A). In this concentration range, binding reaches equilibrium (Lad et al., 2015) before membrane permeabilization in our assay. PF74 slowed the loss of CA from leaky and opening capsids in a concentration-dependent manner, but we observed high levels of stabilisation (loss of less than 10% of signal over the 8 min imaging period) only at high concentrations (≥5 μM, ≥95% occupancy). However, even 10 μM PF74 was unable to prevent CA lattice disassembly over longer periods of time, and we observed ~70% signal loss after 80 min (Figure 8B). PF74 also required high occupancy to accelerate capsid opening, and the drug showed only partial capsid-breaking at a concentration of 1 μM (79–89% occupancy) (Figure 8-Figure Supplement 1).

The FG pocket-binding drug BI-2 also has potent capsid-breaking activity (Márquez et al., 2018) when used at a concentration (50 μM) that is ~40-fold above the K_D (1.2 μM) of the interaction with CA hexamers (Price et al., 2014). We predicted that BI-2 would be unable to stabilise CA lattices after capsid opening since the compound contacts only one of the two CA subunits forming the FG binding pocket (Figure 1A). As expected, CypA paint analysis showed that 50 μM BI-2 did not slow the release of CA subunits from the lattice (Figure 8E). These observations together with those described above suggest that PF74 exerts the same structural effects on the capsid as LEN but less potently, while BI-2 breaks the capsid but is unable to slow subsequent disassembly.

To relate the degree of the capsid-altering effects of PF74 to its effects on HIV infection, we measured the dose-response curve for inhibiting infection of Jurkat cells with VSV-G pseudotyped HIV encoding GFP as a reporter (Figure 8C). To facilitate comparison to the corresponding LEN data, we replotted the dose-response curves as a function of drug concentration divided by the respective affinity to the CA hexamer (Figure 8D). Curves for both drugs showed the characteristic biphasic profile with the first phase levelling off at ~10% infection over a ~10–fold concentration range followed by a second drop in infection. Compared to PF74, the LEN curve was shifted by a factor of 10 to lower concentrations relative to K_D, such that the IC50 for infection occurred at a concentration of ~0.5×K_D and ~5×K_D for LEN and PF74, respectively. Thus, early phase inhibition required 33% occupancy for LEN and 83% occupancy for PF74. Similarly, the second inhibition required a concentration of ~4.7×K_D for LEN (82% occupancy) and ~31×K_D for PF74 (97% occupancy). These data suggest that not only is the second phase of inhibition due to capsid detrimental structural changes, but that LEN has a greater potency for eliciting these changes.

CPSF6 peptide stabilises the CA lattice at low occupancy.

Given that different compounds can influence uncoating mechanisms in different ways, it is conceivable that the virus uses endogenous ligands to tune capsid stability. We therefore sought to compare the effect of the above drugs with CPSF6, a host cell protein which also binds the FG-pocket, and bridges the gap between monomers (Price et al., 2012). CPSF6 colocalises with the capsids at the nuclear pore complex and inside the nucleus where it plays a role in facilitating nuclear entry and dictating integration site position (Bejarano et al., 2019; Schaller et al., 2011; Sowd et al., 2016; Zila et al., 2021). To investigate the effect of CPSF6 on capsid stability, we performed single-molecule TIRF uncoating experiments in the presence of the minimal CPSF6 peptide that binds to the FG pocket (Figure 1D). At 100 μM (2–fold above the KD of 50 μM for binding to CA hexamers), CPSF6 peptide promoted capsid opening, but with slower kinetics than the FG pocket-binding drugs (Figure 9–Figure Supplement 1). CypA paint analysis showed that 100 μM CPSF6 peptide strongly inhibited

CA release (Figure 9A) as evident from slow decay in the CypA paint signal over 80 min (Figure 9C). Further experiments showed that 1 μM CPSF6 peptide was insufficient to stabilise the lattice but 5 μM partially and 10 μM strongly inhibited CA lattice dissociation. Next, we used a TIRF microscopy-based interaction assay to count the number of fluorescently labelled CPSF6 molecules bound to the capsid at concentrations up to 5 μM (measurements at higher concentrations were hampered by high background fluorescence). This analysis showed that on average 278±19 molecules are bound per capsid at 5 μM (Figure 9B and Figure 9–Figure supplement 2). Thus, CPSF6 peptide was more strongly stabilising relative to K_D than capsid inhibitors, providing partial stabilisation when less than 20% of binding sites are occupied.

Discussion

Here we show that the antiretroviral LEN has two opposing effects on the HIV-1 capsid at high occupancy: it prevents dissociation of CA from the lattice but induces capsid rupture. This apparently counterintuitive phenomenon is consistent with a model in which the lattice must be simultaneously stable but flexible. The antiviral mechanism of LEN can therefore be considered a form of 'lethal hyperstability' in which lattice stability is increased at the cost of its flexibility and ultimately capsid integrity. This is reminiscent of the 'lethal mutagenesis' mechanism of antiviral polymerase drugs such as favipiravir (Perales et al., 2011). Just as with capsid stability, viral replication has conflicting requirements – errors are necessary to promote mutagenesis and evolvability (Tokuriki and Tawfik, 2009) but too many errors and fidelity is compromised. Lethal mutagenesis drugs exert their antiviral affects by pushing viral polymerases to these unsustainable error rates. Similarly, lethal hyperstability capsid drugs like LEN push the capsid lattice to such extreme stabilities that the integrity of the capsid is compromised. Importantly, this mechanism dominates at drug doses required to suppress replication to clinically relevant levels (Dvory-Sobol et al., 2022).

Kinetically, the effects of lethal hyperstability occur within minutes and are observable prior to reaching binding equilibrium or full occupancy. We estimate that the threshold for drug-induced capsid rupture and lattice stabilisation is lower than 50% occupancy. The cofactor IP6, which, in the absence of drug, would normally delay spontaneous capsid opening by many hours, raises the threshold to greater ~70% occupancy but is ultimately unable to prevent rapid LEN-induced capsid rupture. Due to the high affinity of the drug, sub-nM concentrations are sufficient to exceed this threshold, but it takes hours to reach the requisite binding level. It is also worth noting that HIV capsids are pleiomorphic and exhibit different levels of intrinsic stability as evident from our single-particle analysis, such that the threshold for LEN-induced structural changes is likely to vary between different capsid architectures.

The comparison of the single-particle analysis of the three major drugs (BI-2, PF74, and LEN) offers insight into how binding stabilises the CA lattice, even when it is no longer a closed shell. BI-2 is the simplest compound, and only makes contacts within a single monomer and has the lowest affinity. As such it offers no potential for enhancing contacts between individual proteins within the lattice. It is therefore unsurprising that, even at 50 μM (approaching the solubility limit of the drug), BI-2 provides no significant lattice stabilisation once the capsid has ruptured. PF74 and LEN, on the other hand, both make contacts across the junction between monomers within the context of the hexamer, and both have been shown to have higher affinity for hexamers than monomers. This suggests that the two drugs lock monomers together within the hexamer, potentially limiting their ability to move with respect to each other - reducing degrees of freedom and hence flexibility within the lattice overall. Evidence that the hexamers are stabilised comes from lattice assembly experiments

in which LEN promotes CA assembly in the presence of IP6 (Figure 6) or high salt (Bester et al., 2020; Link et al., 2020). While PF74 does stabilise the CA lattice post-rupture, the lattice will deteriorate on a time scale of an hour. LEN-treated cores, on the other hand, show no lattice loss even after 5 hours post-rupture. The degree of lattice stabilisation, therefore, correlates with the degree to which the drugs bridge the junction between monomers.

How exactly stabilising the lattice triggers capsid rupture is less clear. It has previously been suggested that the binding of the drug reduces the flexibility of the CA molecule and therefore the lattice plasticity required to maintain capsid integrity (Bhattacharya et al., 2014). These authors also suggest that, due to its hexamer preference, PF74 stabilises hexamers at the cost of pentamers. As precisely 12 pentamers are required, any process that disfavour pentamers, would necessarily lead to capsid rupture. A recent cryoET study comparing the structures of hexamers and pentamers identified residues 58-61 as being a potential 'switch' between the two states (Schirra et al., 2022). Importantly, the pentamer configuration of these residues results in a remodelling of the FG-binding site. The authors speculate that LEN may result in an induced fit switch to the hexameric configuration, and our data would be consistent with such a model. Another cryoET study of HIV cores incubated under conditions that facilitate reverse transcription inside the capsid showed that treatment with GS-CA1 (an analogue of LEN) for 4 hours led to loss of CA lattice pieces and a flattening of the remaining lattice (Christensen et al., 2020). The authors proposed that the compound restricts CA flexibility, causing a build-up of lattice strain, and consequently lattice fracture. We previously proposed a similar mode of action for the capsid-breaking activity of PF74 (Márquez et al., 2018).

Importantly, LEN also possesses antiviral activity during viral production. Not only does LEN compromise the integrity of existing capsid cores but it interferes with assembly/maturation as well. Our *in vitro* assembly experiments suggest that, while LEN promotes IP6-driven assembly it leads to improperly assembled cones that cannot be closed. This is consistent with the observation that LEN (Bester et al., 2020) and the closely related analogue GS-CA1 (Yant et al., 2019) lead to the formation of aberrant capsids in virions. IP6 binds to the electropositive 'pore' created by 6 (or 5) copies of Arg18 at the centre of each CA hexamer (or pentamer). By neutralising the charge repulsion, IP6 stabilises these structures and is thought to be particularly important for incorporation of pentamers (Gupta et al., 2022; Renner et al., 2021) required for forming the high curvature lattice at the ends of the cone. On the other hand, LEN drives assembly of low curvature hexameric lattices (Figure 6B). Both compounds together might lead to uncontrolled lattice growth without the ability to reverse defects and/or LEN might drive remodelling of pentamers at the growing lattice edge into hexamers (Grime et al., 2016). Furthermore, the over-assembly phenotype that we observe upon drug treatment of mature virions supports the notion that LEN both causes aberrant CA assembly and also distorts existing structures. While our data do not resolve how the LEN-induced capsid defects manifest structurally in isolated capsids, within mature virions this could be due to a build-up of strain within the primary capsid. In addition, 'secondary CA lattices' would likely compete for the limited IP6 present within the virion, effectively reducing the amount available to the primary capsid, thereby reducing its resistance to rupture and possibly also adjusting the hexamer/pentamer balance.

The antiviral multimodality of LEN is also seen in the biphasic response curve in the infection assay. The high-dose phase occurs above 0.5 nM LEN, above which the considerations of capsid rupture are relevant. The high-dose phase also corresponds to the concentrations at which reverse transcription is also inhibited. A biphasic inhibition curve has

previously been seen for PF74 (and is repeated here) where, similarly, loss of reverse transcription accompanies this high-dose phase. We and others had previously attributed the loss of reverse transcriptase activity to the opening of the capsid lattice and release of the RT enzyme (Christensen et al., 2020; Jennings et al., 2020; Sowd et al., 2021). Our data support this same explanation for LEN-induced loss of RT. However, LEN is not simply a tighter-binding version of PF74. Figure 8D shows that when the drug response curves are normalised to K_D, LEN exerts its effects at much lower capsid occupancy than PF74. In a previous study, when BI-2 and PF74 were similarly compared, they were found be identical (Price et al., 2014). This suggests that increased CA affinity only partially explains LEN's superior potency and may speak to a greater 'rigidification potential' or ultrastructure-altering capability relative to prior compounds that target this same site.

While the second phase of the dose response curve has a clear explanation, the activity of the drugs at the first phase remains controversial. At these concentrations (<0.5 nM for LEN; <4 nM PF74, <50 nM for BI-2) neither capsid rupture nor loss of viral DNA synthesis are observed. One possible explanation could be that at low drug concentration the low occupancy contributes to CA lattice stability, without the concomitant rupture observed at higher doses. In combination with the cone-stabilising activity of IP6, low dose LEN could render the capsid core too stable thereby leading to altered genome release kinetics during infection. However, the observation that 2-LTR circle formation is not reduced at the EC50 for infection (Bester et al., 2020) is inconsistent with this model as failure to release the viral cDNA from the capsid would be expected as a result of capsid stabilisation. Alternatively, disrupting the ability of the capsid to interact with FG-containing cofactors (Sec24C, Nup153, and CPSF6) has also been proposed to inhibit infection. Our data predict that, at its EC50, LEN occupies approximately one third of the FG-binding sites, while PF74 occupies >80% of sites (Figure 8D). However, the true degree to which these drugs are able to compete with cofactor binding during infection is complicated by the spatial organisation of the cofactors in the cell, the unknown degree to which they compete with each other, the possibility that they exist as high-avidity multimers, and fluctuations in their abundances throughout the cell cycle and between cell types.

The fact that these drugs target a cofactor binding site (the FG pocket) and are capable of modulating capsid rupture and stability raises the question as to whether the virus is employing these cofactors to regulate uncoating. This has previously been suggested for cofactors binding at other CA lattice sites, such as the interactions between CypA and the cyclophilin loop (Rasaiyaah et al., 2013) or between IP6 and the R18 ring (Mallery et al., 2018). The best characterised of the cofactors interacting with the FG pocket is CPSF6, which binds via a linear peptide motif and, like PF74 and LEN makes contacts across the junction between monomers. Our observation that CPSF6 stabilises the CA lattice is consistent with the notion that this bridging interaction promotes stability. A surprising result was the degree to which CPSF6 provided stabilisation, achieving this effect as low as 20% binding sites are occupied. This could indicate that the nature of the bridging interaction is somehow more flexible than those observed for the drugs, leading to differences in the dependence of binding on the curvature of the CA lattice. Indeed, cryoET imaging of CA cones have shown that CPSF6 binding is independent of lattice curvature while PF74 prefers low curvature regions. We acknowledge that we are studying an isolated monomeric peptide motif, while endogenous CPSF6 will likely have a higher binding constant due to avidity, as it is expected to be at least a dimer (Ning et al., 2018), but possibly higher, as CPSF6 has been associated with phase separated condensates within the nucleus (Greig et al., 2020). The nuclear localisation of CPSF6 and the above stabilisation activity, may account for the

observation of capsid remnants in the nucleus discrete from integrated proviral DNA (Müller et al., 2021; Zila et al., 2021).

For decades, the concept that the HIV capsid must release its contents to complete infection has been accepted, and the metastability of the capsid has been recognised as critical for the viral life cycle. LEN is the first capsid-targeting drug for treatment of HIV infection. Our work here shows that LEN functions by lethal hyperstabilisation, and that this is a powerful mechanism for achieving multi-log impacts on viral infectivity. As such, this mechanism and the tools that we and others have developed for studying it will likely be relevant to the development of new therapeutics targeting a range of viral infections. Furthermore, LEN reveals that FG-pocket binding can drastically alter the capsid integrity. The exact nature of the induced ultrastructural defect warrants further study, as does the role of single and multiple endogenous cofactors on the uncoating process.

Materials and Methods

Production of GFP-loaded HIV particles for TIRF uncoating experiments

HIV particles lacking envelope protein were produced, biotinylated and purified as described (Márquez et al., 2019). Briefly, HEK293T cells were transfected using PEI with a mixture of the plasmids pNL4.3-iGFP-ΔEnv and psPAX2 (1.4:1, mol/mol) to produce GFP-loaded HIV particles or with a mixture of pCRV1-GagPol and pCSGW (1:1.7, mol/mol) to produce dark HIV particles. The medium was exchanged 18 h post transfection and the virus-containing medium was collected 72 hours post transfection and centrifuged (2100 x g, 20 min, 4 °C) to remove cells. The viral particles were then biotinylated using EZ-Link Sulfo-NHS-LC-LC-Biotin and purified by size exclusion chromatography.

Expression and purification of DLY

The gene encoding the pore-forming protein desulfolysin (DLY) was subcloned by ligation independent cloning into the pMCSG7 vector from the pET22b construct described in (Hotze et al., 2013) to introduce an N-terminal His-tag. DLY was expressed in *E. coli* BL21(DE3) pREP4 cells in TB media with Ampicillin (100 mg/mL) by induction with 0.2 mM IPTG at 37 °C with shaking for 4 hours. Cells were harvested by centrifugation and lysed in 20 mM Tris pH 7.2 300 mM NaCl buffer with 10% glycerol, protease inhibitor, 0.1% Triton-X100, DNAse and lysozyme for 1 hour at room temperature. The lysate was clarified by centrifugation and passed over a HisTrap™ HP column (Cytiva Life Sciences) equilibrated in 20 mM Tris pH 7.2, 300 mM NaCl and 5% glycerol. DLY was elutded over a linear gradient of 0–500 mM imidazole. The eluted protein was further purified by size exclusion chromatography on a HiLoad 16/60 Superdex 200 pg column (Cytiva Life Sciences) preequilibrated with 20 mM Tris pH 7.2, 300 mM NaCl, 5% glycerol, 0.5 mM DTT.

Expression and purification of CypA

Human CypA was expressed in BL21(DE3) *E. coli* for 3 h after IPTG induction in LB medium at 37 °C with shaking. Cells were harvested by centrifugation and lysed by sonication on ice in a buffer containing 25 mM HEPES, pH 7.6, 1 mM DTT, 0.02% NaN_3, 'Complete' protease inhibitor and 1 mg mL^{-1} lysozyme. The lysate was clarified by centrifugation. CypA was purified by subtractive anion exchange chromatography using a 10 mL HiTrap Q HP column (GE Healthcare Life Science) equilibrated with 25 mM HEPES, pH 7.6, 1 mM DTT, 0.02% NaN_3. CypA fractions eluting in the flow-through were adjusted to pH of with 1% v/v acetic acid, centrifuged and applied to a cation exchange chromatography column (5 mL HiTrap SP HP, GE Healthcare Life Science) equilibrated with 25 mM sodium phosphate, pH 5.8, 1 mM DTT, 0.02% NaN_3. CypA was eluted with a linear gradient from 0 to 1 M NaCl over 20 column volumes. CypA was dialyzed against storage buffer (25 mM MOPS, pH 6.6, 1 mM DTT, 0.02% NaN_3), concentrated using an Amicon-15 Ultra centrifugal filtration device (10 k MWCO, Merck) and frozen in liquid nitrogen for storage at -80 °C.

Labelling of CypA

CypA was dialysed against PBS (pH 7.4, 0.1 mM TCEP) and labeled by reaction with a 4-fold molar excess of Alexa-Fluor 568-C5-maleimide (Thermo Fisher Scientific, A10254) for 10 minutes at room temperature. The reaction was quenched by addition of DTT. Labeled CypA was separated from unconjugated dye using Zeba desalting spin columns (Thermo Fisher Scientific) equilibrated with 50 mM Tris, pH 7.9, 20% v/v glycerol, 1 mM DTT. Under these conditions, CypA is quantitatively labeled at residue C51. Labeled CypA was frozen in liquid nitrogen and stored at -40 °C.

CPSF6 peptides

The peptides $CPSF6_{313–327}$ (CPSF6p) and $CPSF6_{313–327}$ with an extra cysteine at the C-terminus (CPSF6p-Cys) were synthetized by GenScript. Peptides were dissolved in water at a concentration of 2.5 mM and stored in aliquots at -40°C.

Labelling of CPSF6 peptide

CPSF6p-Cys was labelled with Alexa-Fluor 568-C5-maleimide (Thermo Fisher Scientific) added at an equimolar ratio in HEPES buffer pH 8. Labelling was verified by thin layer chromatography (TLC). No unconjugated dye was observed on TLC. CPSF6p-Cys- AF568 solution stored in aliquots at -40°C.

Single-molecule TIRF uncoating assay

Single-molecule imaging of viral particles was carried out using TIRF microscopy with microfluidic sample delivery according to our previously published methods (Márquez et al., 2019). Briefly, biotinylated viral particles were captured onto coverslips attached to PDMS microfluidic flow cells and imaged using a custom-built TIRF microscope with an ASI-RAMM frame (Applied Scientific Instrumentation), a Nikon 100× CFI Apochromat TIRF (1.49 NA) oil immersion objective and NicoLase laser system (Nicovich et al., 2017). Immobilized virions were treated with imaging buffer containing 200 nM pore forming protein (DLY or SLO) to permeabilize viral membrane and AF568-labeled CypA (0.8 μM) to paint the capsid. Drugs (LEN, PF74, BI-2) were added to the imaging buffer as stock solutions in DMSO (final concentration not exceeding 0.5%). Images were acquired at a rate of 1 frame per 6 s for 30 minutes unless specified otherwise.

TIRF image analysis

Single-virion fluorescence traces were extracted from the TIRF image stacks using the JIM Immobilized Microscopy analysis package and further analyzed in MATLAB (The MathWorks Inc.). *Capsid opening via GFP release:* Change-point analysis of GFP intensity traces was used to identify the presence and time of steps corresponding to membrane permeabilization and capsid opening. Traces were automatically sorted into four classes on the basis of the following criteria: (1) loss of entire GFP signal in one step; (2) loss of GFP intensity in one large (permeabilization) and one small (capsid opening) step; (3) loss of the majority of the GFP signal in one step with residual GFP signal persisting for the rest of the experiment; (4) no permeabilization or otherwise uninterpretable traces (excluded from analysis). Capsid opening times were calculated for traces in class two as the time difference between permeabilization and capsid opening. Survival curves were constructed from the pooled opening times acquired in independent uncoating experiments. *Analysis of CA lattice stability via CypA paint:* Heatmaps and median traces of leaky or closed particles were generated after aligning at traces in the corresponding category at the time of membrane permeabilization. Traces of opening particles were aligned at the time of membrane permeabilization (shown in the first panel) and aligned at the time of capsid opening (shown in the second panel). *Quantification bound molecules:* The number of bound AF568-labelled CPSF6p molecules was determined from the ratio of the CPSF6p-AF568 fluorescence intensity associated with the capsid at equilibrium to the fluorescence intensity of a single CPSF6p-AF568 molecule.

Production of pseudotyped-virus particles for cell-based assays

VSV-G pseudotyped GFP-encoding virus particles were generated by co-transfecting HEK293T cells with pCRV1-GagPol, pCSGW and pMD2.G (1:1.1:1.3 mol/mol) using PEI 25K. The culture medium was removed 16 hours post-transfection and replenished with a

fresh medium containing 10 mM $MgCl_2$, 0.5 mM $CaCl_2$ and 100 U of DNase. Virus-containing medium was harvested 72 hours post-transfection, centrifuged (2100 x g, 20 min, 4°C) to remove cell debris, divided into aliquots and stored at -80°C.

Infection assays

Infection assays were performed in 96 well plates using 0.75 x 10^5 Jurkat cells per well pre-treated with the indicated drug (LEN, PF74) concentrations for 30 minutes at 37°C. The cells were then infected in triplicate with VSV-G-pseudotyped GFP-encoding virus in the presence of polybrene (10 µg/ml; Sigma) at room temperature for 20 minutes, followed by spinoculation at 800 x g for 1 hour at room temperature. The culture media were removed and replenished with fresh media containing drugs at the indicated concentrations. At 48 hours post infection, the cells were fixed in 2% paraformaldehyde (Electron Microscopy Sciences) for 1 hour at room temperature and analyzed by flow cytometry using a LSRFortessa cell analyzer (BD Biosciences) and FlowJo software. For experiments involving preincubation with drugs, the virus was incubated with LEN at the indicated concentrations for 48 hours at room temperature and then used to infect cells as above. For quantitative PCR (qPCR) analysis, virus was treated with DNase for 30 minutes at 37°C and then used to infect 1 x 10^5 Jurkat cells in duplicate as described above. Cells were harvested 24 hours post infection and processed for qPCR.

Quantitative PCR analysis

Genomic DNA was isolated from pelleted cells using a DNeasy blood and tissue kit (Qiagen). The concentration of purified DNA was determined using a Nanodrop spectrophotometer. To quantify total viral DNA, quantitative PCR was performed using sequence-specific primers and SsoAdvanced Universal SYBR Green Supermix (Bio-Rad). For 2-LTR circles, quantitative PCR was performed using sequence-specific primers, TaqMan probes (Thermo Fisher Scientific) and iQ Supermix (Bio-Rad). PCR conditions for vDNA amplification: Initial denaturation, 95°C, 3 min; Denaturation, 95°C, 10 s; Annealing/Extension, 60°C, 30 s; 45 cycles. PCR conditions for 2-LTR amplification: Initial denaturation, 95°C, 3 min; Denaturation, 95°C, 15 s; Annealing/Extension, 60°C, 60 s; 50 cycles.

Expression and purification of CA for in vitro assembly experiments

E. coli C41 cells expressing CA were lysed and cell debris was removed by centrifugation. CA was precipitated by addition of 25% ammonium sulphate to the supernatant, collected by centrifugation, resuspended, and dialysed against 50 mM MES (pH 6.0), 20 mM NaCl, 1 mM DTT. The CA protein was further purified on a cation exchange column with a gradient from 20 mM to 1 M NaCl followed by size exclusion chromatography with Tris pH 8.0, 20 mM NaCl, 1 mM DTT and finally snap frozen.

Turbidity assay to measure CA assembly kinetics

CA proteins were dialysed against 50 mM MES (pH 6.0), 1 mM DTT. CA proteins were assembled at a final concentration of 75 µM in the presence of 2% DMSO. LEN titration: LEN (final concentration between 0.5–50 µM) was added to the CA solution and assembly was initiated by adding IP6 (final concentration of 200 µM). IP6 titration: IP6 (final concentration between 50–150 µM) ±LEN (final concentration 50 µM) was added to the CA solution to induce assembly. The increase in Abs_{350} was measured with a PHERAstar FSX Plate reader (BMG Labtech) in 384-well plate every 22 s with shaking after each measurement.

Treatment of self-assembled CA cones with LEN

CA cones were assembled by adding IP6 (final concentration of 1 mM) to a solution of CA (final concentration of 75 µM) in 50 mM MES (pH 6.0) and incubating the reaction mixture for 2 h. LEN (final concentration of 50 µM) was added and the CA cones and the mixture was applied to an EM grid for negative staining with uranyl acetate at the indicated time points.

Negative staining EM of self-assembled CA structures

The samples from the turbidity assay were allowed to sediment overnight. Then 5 µL of each sample was applied to a carbon coated grid (Cu, 400 mesh, Electron Microscopy Services) previously cleaned by glow discharge. The grids were then washed, and samples stained with 2% uranyl-acetate. Micrographs were taken at room temperature on a Tecnai Spirit (FEI) operated at an accelerated voltage of 120 keV and recorded with a Gatan 2k × 2k CCD camera. Images were collected with a total dose of ~30 $e^-/Å^2$ and a defocus of 1–3 µm.

HIV particle production for cryo-electron tomography

Replication deficient VSV-G pseudotyped HIV-1 virions were produced in HEK293T cells using pCRV1-GagPol, pCSGW and pMD2.G as described previously (Price et al., 2014). At 24–48 h post transfection, the supernatants were harvested and passed through 0.22 µm nitrocellulose filter. The virions were concentrated by ultracentrifugation through a 20% (w/v) sucrose cushion (2 h at 28,000 rpm in a SW32 rotor [Beckman Coulter Life Sciences]). The pellet was resuspended in PBS, snap-frozen and stored at -80 °C. LEN-treated virions were incubated in presence of 700 nM LEN for 1.5 h at room temperature prior to plunge-freezing for cryo-ET.

Cryo-electron tomography of LEN-treated HIV particles

Colloidal gold beads (10 nm diameter) were added to the purified HIV particles and 6 µl of this suspension was applied to a C-Flat 2/2 3C grid cleaned by glow discharge (20 mA, 40 s). The grids were blotted and plunge-frozen in liquid ethane using an FEI Vitrobot Mark II at 16 °C and 100% humidity. Tomographic tilt series between −40° and +40° with increments of 3°, defoci between -3 µm and -6 µm at a magnification of 50,000x were acquired using Serial-EM (Mastronarde, 2005) on a TF2 Tecnai F20 transmission electron microscope under low-dose conditions at 200 kV and images recorded with a Falcon III direct electron detector. The Imod package (IMOD Version 4.9.0) was used to generate tomograms (Kremer et al., 1996). The alignment of 2D projection images of the tilt series was done using gold particles as fiducial markers. A 3D reconstruction was generated using back projection of the tilt-series.

Acknowledgements

This work was supported by NHMRC Ideas Grant APP1182212 (DAJ, TB), Wellcome Trust Collaborator Award 214344/Z/18/Z (GJT, LJ, DAJ, TB), NHMRC Investigator Grant APP1194263 (MWP), Australian Research Council Grants DP160101874 and DP200102871 (MWP) and a UNSW Scientia Award (KMRF). CM received an Australian Government Research Training Program Scholarship. Infrastructure support from the NHMRC Independent Research Institutes Infrastructure Support Scheme and the Victorian State Government Operational Infrastructure Support Program to St. Vincent's Institute are gratefully acknowledged. MWP is an NHMRC Leadership Fellow. We thank Sara Lawrence (St. Vincent's Institute) for expression and purification of recombinant DLY, Claire Dickson and Prabhjeet Phalora for critical feedback on the manuscript.

Author contributions

K.M. Rifat Faysal: Methodology; Investigation; Formal analysis; Writing-Original draft.
Nadine Renner: Investigation; Formal analysis; Writing–review and editing
Chantal Márquez: Investigation; Formal analysis; Writing–review and editing
Vaibhav Shah: Investigation; Formal analysis; Writing–review and editing
Andrew Tuckwell: Formal analysis; Writing–review and editing
Michelle Christie: Resources; Writing–review and editing
Michael Parker: Resources; Writing–review and editing; Supervision; Funding acquisition
Stuart Turville: Resources; Writing–review and editing; Supervision; Funding acquisition
Greg Towers: Writing–review and editing; Funding acquisition
Leo James: Writing–review and editing; Supervision; Funding acquisition
David Jacques: Conceptualisation; Writing–original draft; Supervision; Funding acquisition
Till Böcking: Conceptualisation; Methodology; Writing–original draft; Supervision; Funding acquisition

ORCID IDs

K.M. Rifat Faysal:
Nadine Renner:
Chantal Márquez: 000-0002-3935-4554
Vaibhav Shah: 0000-0002-9123-0180
Andrew Tuckwell: 0000-0002-8940-7768
Michelle Christie: 0000-0002-7001-3400
Michael Parker: 0000-0002-3101-1138
Stuart Turville: 0000-0003-1918-5343
Greg Towers: 0000-0002-7707-0264
Leo James: 0000-0003-2131-0334
David Jacques: 000-0002-6426-4510
Till Böcking: 0000-0003-1165-3122

References

Alvarez LZ, Govasli ML, Rasaiyaah J, Monit C, Perry SO, Sumner RP, McAlpine-Scott S, Dickson C, Faysal KMR, Hilditch L, Miles RJ, Bibollet-Ruche F, Hahn BH, Boecking T, Pinotsis N, James LC, Jacques DA, Towers GJ. 2022. Macrophage activation of cGAS and TRIM5 distinguish pandemic and non-pandemic HIV. *Biorxiv* 2022.01.21.477263. doi:10.1101/2022.01.21.477263

Bejarano DA, Peng K, Laketa V, Börner K, Jost KL, Lucic B, Glass B, Lusic M, Müller B, Kräusslich H-G. 2019. HIV-1 nuclear import in macrophages is regulated by CPSF6-capsid interactions at the nuclear pore complex. *Elife* 8:e41800. doi:10.7554/elife.41800

Bester SM, Wei G, Zhao H, Adu-Ampratwum D, Iqbal N, Courouble VV, Francis AC, Annamalai AS, Singh PK, Shkriabai N, Blerkom PV, Morrison J, Poeschla EM, Engelman AN, Melikyan GB, Griffin PR, Fuchs JR, Asturias FJ, Kvaratskhelia M. 2020. Structural and mechanistic bases for a potent HIV-1 capsid inhibitor. *Sci New York N Y* 370:360–364. doi:10.1126/science.abb4808

Bhattacharya A, Alam SL, Fricke T, Zadrozny K, Sedzicki J, Taylor AB, Demeler B, Pornillos O, Ganser-Pornillos BK, Diaz-Griffero F, Ivanov DN, Yeager M. 2014. Structural basis of HIV-1 capsid recognition by PF74 and CPSF6. *Proceedings of the National Academy of Sciences* 111:18625–18630. doi:10.1073/pnas.1419945112

Blair WS, Pickford C, Irving SL, Brown DG, Anderson M, Bazin R, Cao J, Ciaramella G, Isaacson J, Jackson L, Hunt R, Kjerrstrom A, Nieman JA, Patick AK, Perros M, Scott AD, Whitby K, Wu H, Butler SL. 2010. HIV Capsid is a Tractable Target for Small Molecule Therapeutic Intervention. *PLoS Pathogens* 6. doi:10.1371/journal.ppat.1001220

Bunce CM, French PJ, Allen P, Mountford JC, Moor B, Greaves MF, Michell RH, Brown G. 1993. Comparison of the levels of inositol metabolites in transformed haemopoietic cells and their normal counterparts. *Biochem J* 289:667–673. doi:10.1042/bj2890667

Christensen DE, Ganser-Pornillos BK, Johnson JS, Pornillos O, Sundquist WI. 2020. Reconstitution and visualization of HIV-1 capsid-dependent replication and integration in vitro. *Sci New York N Y* 370. doi:10.1126/science.abc8420

Dick RA, Zadrozny KK, Xu C, Schur FKM, Lyddon TD, Ricana CL, Wagner JM, Perilla JR, Ganser-Pornillos BK, Johnson MC, Pornillos O, Vogt VM. 2018. Inositol phosphates are assembly co-factors for HIV-1. *Nature* 560:1. doi:10.1038/s41586-018-0396-4

Dvory-Sobol H, Shaik N, Callebaut C, Rhee MS. 2022. Lenacapavir: a first-in-class HIV-1 capsid inhibitor. *Curr Opin Hiv Aids* 17:15–21. doi:10.1097/coh.0000000000000713

Fontana J, Keller PW, Urano E, Ablan SD, Steven AC, Freed EO. 2016. Identification of an HIV-1 Mutation in Spacer Peptide 1 That Stabilizes the Immature CA-SP1 Lattice. *J Virol* 90:972–978. doi:10.1128/jvi.02204-15

Fricke T, Buffone C, Opp S, Valle-Casuso J, Diaz-Griffero F. 2014. BI-2 destabilizes HIV-1 cores during infection and Prevents Binding of CPSF6 to the HIV-1 Capsid. *Retrovirology* 11:1–7. doi:10.1186/s12977-014-0120-x

Ganser BK, Li S, Klishko VY, Finch JT, Sundquist WI. 1999. Assembly and analysis of conical models for the HIV-1 core. *Science (New York, NY)* 283:80–3. doi:10.1126/science.283.5398.80

Greig JA, Nguyen TA, Lee M, Holehouse AS, Posey AE, Pappu RV, Jedd G. 2020. Arginine-Enriched Mixed-Charge Domains Provide Cohesion for Nuclear Speckle Condensation. *Mol Cell* 77:1237-1250.e4. doi:10.1016/j.molcel.2020.01.025

931 Grime JM, Dama JF, Ganser-Pornillos BK, Woodward CL, Jensen GJ, Yeager M, Voth GA. 2016.
932 Coarse-grained simulation reveals key features of HIV-1 capsid self-assembly. *Nature*
933 *communications* 7:11568. doi:10.1038/ncomms11568

934 Gupta M, Pak AJ, Voth GA. 2022. Critical Mechanistic Role of Inositol Hexakisphosphate (IP6) in HIV-
935 1 Viral Capsid Assembly. *Biorxiv* 2022.05.03.490470. doi:10.1101/2022.05.03.490470

936 Hori T, Takeuchi H, Saito H, Sakuma R, Inagaki Y, Yamaoka S. 2013. A Carboxy-Terminally
937 Truncated Human CPSF6 Lacking Residues Encoded by Exon 6 Inhibits HIV-1 cDNA Synthesis
938 and Promotes Capsid Disassembly. *Journal of Virology* 87:7726–7736. doi:10.1128/jvi.00124-13

939 Hotze EM, Le HM, Sieber JR, Bruxvoort C, McInerney MJ, Tweten RK. 2013. Identification and
940 Characterization of the First Cholesterol-Dependent Cytolysins from Gram-Negative Bacteria.
941 *Infect Immun* 81:216–225. doi:10.1128/iai.00927-12

942 Huang P-T, Summers BJ, Xu C, Perilla JR, Malikov V, Naghavi MH, Xiong Y. 2019. FEZ1 Is Recruited
943 to a Conserved Cofactor Site on Capsid to Promote HIV-1 Trafficking. *Cell Reports*.
944 doi:10.1016/j.celrep.2019.07.079

945 Hulme AE, Kelley Z, Foley D, Hope TJ. 2015. Complementary Assays Reveal a Low Level of CA
946 Associated with Viral Complexes in the Nuclei of HIV-1-Infected Cells. *Journal of virology*
947 89:5350–61. doi:10.1128/jvi.00476-15

948 Jacques DA, McEwan WA, Hilditch L, Price AJ, Towers GJ, James LC. 2016. HIV-1 uses dynamic
949 capsid pores to import nucleotides and fuel encapsidated DNA synthesis. *Nature* 536:349–53.
950 doi:10.1038/nature19098

951 Jennings J, Shi J, Varadarajan J, Jamieson PJ, Aiken C. 2020. The Host Cell Metabolite Inositol
952 Hexakisphosphate Promotes Efficient Endogenous HIV-1 Reverse Transcription by Stabilizing the
953 Viral Capsid. *Mbio* 11. doi:10.1128/mbio.02820-20

954 Kim K, Dauphin A, Komurlu S, McCauley SM, Yurkovetskiy L, Carbone C, Diehl WE, Strambio-De-
955 Castillia C, Campbell EM, Luban J. 2019. Cyclophilin A protects HIV-1 from restriction by human
956 TRIM5α. *Nat Microbiol* 4:1–8. doi:10.1038/s41564-019-0592-5

957 Kremer JR, Mastronarde DN, McIntosh JR. 1996. Computer Visualization of Three-Dimensional
958 Image Data Using IMOD. *J Struct Biol* 116:71–76. doi:10.1006/jsbi.1996.0013

959 Lad L, Clancy S, Koditek D, Wong MH, Jin D, Niedziela-Majka A, Papalia GA, Hung M, Yant S,
960 Somoza JR, Hu E, Chou C, Tse W, Halcomb R, Sakowicz R, Pagratis N. 2015. Functional Label-
961 Free Assays for Characterizing the in Vitro Mechanism of Action of Small Molecule Modulators of
962 Capsid Assembly. *Biochemistry-us* 54:2240–2248. doi:10.1021/acs.biochem.5b00151

963 Lahaye X, Satoh T, Gentili M, Cerboni S, Conrad C, Hurbain I, Marjou AE, Lacabaratz C, Lelièvre J-
964 DD, Manel N. 2013. The capsids of HIV-1 and HIV-2 determine immune detection of the viral
965 cDNA by the innate sensor cGAS in dendritic cells. *Immunity* 39:1132–42.
966 doi:10.1016/j.immuni.2013.11.002

967 Lamorte L, Titolo S, Lemke CT, Goudreau N, Mercier J-FF, Wardrop E, Shah VB, Schwedler UK von,
968 Langelier C, Banik SS, Aiken C, Sundquist WI, Mason SW. 2013. Discovery of novel small-
969 molecule HIV-1 replication inhibitors that stabilize capsid complexes. *Antimicrobial agents and*
970 *chemotherapy* 57:4622–31. doi:10.1128/aac.00985-13

971 Lee K, Ambrose Z, Martin TD, Oztop I, Mulky A, Julias JG, Vandegraaff N, Baumann JG, Wang R,
972 Yuen W, Takemura T, Shelton K, Taniuchi I, Li Y, Sodroski J, Littman DR, Coffin JM, Hughes SH,
973 Unutmaz D, Engelman A, KewalRamani VN. 2010. Flexible Use of Nuclear Import Pathways by
974 HIV-1. *Cell Host & Microbe* 7. doi:10.1016/j.chom.2010.02.007

975 Letcher AJ, Schell MJ, Irvine RF. 2008. Do mammals make all their own inositol hexakisphosphate?
976 *Biochem J* 416:263–270. doi:10.1042/bj20081417

977 Link JO, Rhee MS, Tse WC, Zheng J, Somoza JR, Rowe W, Begley R, Chiu A, Mulato A, Hansen D,
978 Singer E, Tsai LK, Bam RA, Chou C-H, Canales E, Brizgys G, Zhang JR, Li J, Graupe M,
979 Morganelli P, Liu Q, Wu Q, Halcomb RL, Saito RD, Schroeder SD, Lazerwith SE, Bondy S, Jin D,
980 Hung M, Novikov N, Liu X, Villaseñor AG, Cannizzaro CE, Hu EY, Anderson RL, Appleby TC, Lu
981 B, Mwangi J, Liclican A, Niedziela-Majka A, Papalia GA, Wong MH, Leavitt SA, Xu Y, Koditek D,
982 Stepan GJ, Yu H, Pagratis N, Clancy S, Ahmadyar S, Cai TZ, Sellers S, Wolckenhauer SA, Ling J,
983 Callebaut C, Margot N, Ram RR, Liu Y-P, Hyland R, Sinclair GI, Ruane PJ, Crofoot GE, McDonald
984 CK, Brainard DM, Lad L, Swaminathan S, Sundquist WI, Sakowicz R, Chester AE, Lee WE, Daar
985 ES, Yant SR, Cihlar T. 2020. Clinical targeting of HIV capsid protein with a long-acting small
986 molecule. *Nature* 584:1–5. doi:10.1038/s41586-020-2443-1

987 Mallery DL, Kleinpeter AB, Renner N, Faysal KMR, Novikova M, Kiss L, Wilson MSC, Ahsan B, Ke Z,
988 Briggs JAG, Saiardi A, Böcking T, Freed EO, James LC. 2021. A stable immature lattice packages
989 IP6 for HIV capsid maturation. *Sci Adv* 7:eabe4716. doi:10.1126/sciadv.abe4716

990 Mallery DL, Márquez CL, McEwan WA, Dickson C, Jacques DA, Anandapadamanaban M, Bichel K,
991 Towers GJ, Saiardi A, Böcking T, James LC. 2018. IP6 is an HIV pocket factor that prevents
992 capsid collapse and promotes DNA synthesis. *eLife* 7:e35335. doi:10.7554/eLife.35335

993 Márquez C, Lau D, Walsh J, Faysal KMR, Parker M, Turville S, Böcking T. 2019. Fluorescence
994 Microscopy Assay to Measure HIV-1 Capsid Uncoating Kinetics in vitro. *Bio-protocol* 9:e3297.
995 doi:10.21769/bioprotoc.3297

996 Márquez CL, Lau D, Walsh J, Shah V, McGuinness C, Wong A, Aggarwal A, Parker MW, Jacques
997 DA, Turville S, Böcking T. 2018. Kinetics of HIV-1 capsid uncoating revealed by single-molecule
998 analysis. *eLife* 7. doi:10.7554/eLife.34772

999 Mastronarde DN. 2005. Automated electron microscope tomography using robust prediction of
1000 specimen movements. *J Struct Biol* 152:36–51. doi:10.1016/j.jsb.2005.07.007

1001 Matreyek KA, Yücel SS, Li X, Engelman A. 2013. Nucleoporin NUP153 Phenylalanine-Glycine Motifs
1002 Engage a Common Binding Pocket within the HIV-1 Capsid Protein to Mediate Lentiviral
1003 Infectivity. *Plos Pathog* 9:e1003693. doi:10.1371/journal.ppat.1003693

1004 Mattei S, Anders M, Konvalinka J, Kräusslich H-G, Briggs JA, Müller B. 2014. Induced maturation of
1005 human immunodeficiency virus. *J Virol* 88:13722–31. doi:10.1128/jvi.02271-14

1006 Miles RJ, Kerridge C, Hilditch L, Monit C, Jacques DA, Towers GJ. 2020. MxB sensitivity of HIV-1 is
1007 determined by a highly variable and dynamic capsid surface. *Elife* 9:e56910.
1008 doi:10.7554/elife.56910

1009 Müller TG, Zila V, Peters K, Schifferdecker S, Stanic M, Lucic B, Laketa V, Lusic M, Müller B,
1010 Kräusslich H-G. 2021. HIV-1 uncoating by release of viral cDNA from capsid-like structures in the
1011 nucleus of infected cells. *Elife* 10:e64776. doi:10.7554/elife.64776

1012 Nicovich PR, Walsh J, Böcking T, Gaus K. 2017. NicoLase—An open-source diode laser combiner,
1013 fiber launch, and sequencing controller for fluorescence microscopy. *Plos One* 12:e0173879.
1014 doi:10.1371/journal.pone.0173879

1015 Ning J, Zhong Z, Fischer DK, Harris G, Watkins SC, Ambrose Z, Zhang P. 2018. Truncated CPSF6
1016 Forms Higher-Order Complexes That Bind and Disrupt HIV-1 Capsid. *Journal of Virology*
1017 92:e00368-18. doi:10.1128/JVI.00368-18

1018 Obr M, Schur FKM, Dick RA. 2021. A Structural Perspective of the Role of IP6 in Immature and
1019 Mature Retroviral Assembly. *Viruses* 13:1853. doi:10.3390/v13091853

1020 Peng K, Muranyi W, Glass B, Laketa V, Yant SR, Tsai L, Cihlar T, Müller B, Kräusslich H-G. 2014.
1021 Quantitative microscopy of functional HIV post-entry complexes reveals association of replication
1022 with the viral capsid. *Elife* 3:e04114. doi:10.7554/elife.04114

1023 Pornillos O, Ganser-Pornillos BK, Yeager M. 2011. Atomic-level modelling of the HIV capsid. *Nature*
1024 469:424–427. doi:10.1038/nature09640

1025 Price AJ, Fletcher AJ, Schaller T, Elliott T, Lee K, KewalRamani VN, Chin JW, Towers GJ, James LC.
1026 2012. CPSF6 defines a conserved capsid interface that modulates HIV-1 replication. *PLoS*
1027 *pathogens* 8:e1002896. doi:10.1371/journal.ppat.1002896

1028 Price AJ, Jacques DA, McEwan WA, Fletcher AJ, Essig S, Chin JW, Halambage UD, Aiken C, James
1029 LC. 2014. Host Cofactors and Pharmacologic Ligands Share an Essential Interface in HIV-1
1030 Capsid That Is Lost upon Disassembly. *PLoS Pathogens* 10:e1004459.
1031 doi:10.1371/journal.ppat.1004459

1032 Rankovic S, Ramalho R, Aiken C, Rousso I. 2018. PF74 reinforces the HIV-1 capsid to impair reverse
1033 transcription-induced uncoating. *Journal of Virology* JVI.00845-18. doi:10.1128/jvi.00845-18

1034 Rasaiyaah J, Tan CP, Fletcher AJ, Price AJ, Blondeau C, Hilditch L, Jacques DA, Selwood DL,
1035 James LC, Noursadeghi M, Towers GJ. 2013. HIV-1 evades innate immune recognition through
1036 specific cofactor recruitment. *Nature* 503:402–405. doi:10.1038/nature12769

1037 Rebensburg SV, Wei G, Larue RC, Lindenberger J, Francis AC, Annamalai AS, Morrison J, Shkriabai
1038 N, Huang S-W, KewalRamani V, Poeschla EM, Melikyan GB, Kvaratskhelia M. 2021. Sec24C is
1039 an HIV-1 host dependency factor crucial for virus replication. *Nat Microbiol* 1–10.
1040 doi:10.1038/s41564-021-00868-1

1041 Renner N, Mallery DL, Faysal KMR, Peng W, Jacques DA, Böcking T, James LC. 2021. A lysine ring
1042 in HIV capsid pores coordinates IP6 to drive mature capsid assembly. *Plos Pathog* 17:e1009164.
1043 doi:10.1371/journal.ppat.1009164

1044 Saito A, Ferhadian D, Sowd GA, Serrao E, Shi J, Halambage UD, Teng S, Soto J, Siddiqui MA,
1045 Engelman AN, Aiken C, Yamashita M. 2016. Roles of Capsid-Interacting Host Factors in
1046 Multimodal Inhibition of HIV-1 by PF74. *J Virol* 90:5808–23. doi:10.1128/jvi.03116-15

1047 Santos CDS, Tartour K, Cimarelli A. 2016. A Novel Entry/Uncoating Assay Reveals the Presence of
1048 at Least Two Species of Viral Capsids During Synchronized HIV-1 Infection. *Plos Pathog*
1049 12:e1005897. doi:10.1371/journal.ppat.1005897

1050 Schaller T, Ocwieja KE, Rasaiyaah J, Price AJ, Brady TL, Roth SL, Hué S, Fletcher AJ, Lee K,
1051 KewalRamani VN, Noursadeghi M, Jenner RG, James LC, Bushman FD, Towers GJ. 2011. HIV-1
1052 Capsid-Cyclophilin Interactions Determine Nuclear Import Pathway, Integration Targeting and
1053 Replication Efficiency. *PLoS Pathogens* 7:e1002439. doi:10.1371/journal.ppat.1002439

1054 Schirra RT, Santos NFB dos, Zadrozny KK, Kucharska I, Ganser-Pornillos BK, Pornillos O. 2022. A
1055 molecular switch modulates assembly and host factor binding of the HIV-1 capsid. *Biorxiv*
1056 2022.08.25.505312. doi:10.1101/2022.08.25.505312

1057 Selyutina A, Hu P, Miller S, Simons LM, Yu HJ, Hultquist JF, Lee K, KewalRamani VN, Diaz-Griffero
1058 F. 2022. GS-CA1 and lenacapavir stabilize the HIV-1 core and modulate the core interaction with
1059 cellular factors. *Iscience* 25:103593. doi:10.1016/j.isci.2021.103593

Shi J, Zhou J, Shah VB, Aiken C, Whitby K. 2011. Small-Molecule Inhibition of Human Immunodeficiency Virus Type 1 Infection by Virus Capsid Destabilization. *Journal of Virology* 85:542–549. doi:10.1128/JVI.01406-10

Sowd GA, Aiken C. 2021. Inositol phosphates promote HIV-1 assembly and maturation to facilitate viral spread in human CD4+ T cells. *Plos Pathog* 17:e1009190. doi:10.1371/journal.ppat.1009190

Sowd GA, Serrao E, Wang H, Wang W, Fadel HJ, Poeschla EM, Engelman AN. 2016. A critical role for alternative polyadenylation factor CPSF6 in targeting HIV-1 integration to transcriptionally active chromatin. *Proc National Acad Sci* 113:E1054–E1063. doi:10.1073/pnas.1524213113

Sowd GA, Shi J, Aiken C. 2021. HIV-1 CA inhibitors are antagonized by inositol phosphate stabilization of the viral capsid in cells. *J Virol* JVI0144521. doi:10.1128/jvi.01445-21

Temple J, Tripler TN, Shen Q, Xiong Y. 2020. A snapshot of HIV-1 capsid–host interactions. *Curr Res Struct Biology* 2:222–228. doi:10.1016/j.crstbi.2020.10.002

Towers GJ, Hatziioannou T, Cowan S, Goff SP, Luban J, Bieniasz PD. 2003. Cyclophilin A modulates the sensitivity of HIV-1 to host restriction factors. *Nat Med* 9:1138–1143. doi:10.1038/nm910

Veiga N, Torres J, Domínguez S, Mederos A, Irvine RF, Díaz A, Kremer C. 2006. The behaviour of myo-inositol hexakisphosphate in the presence of magnesium(II) and calcium(II): Protein-free soluble InsP6 is limited to 49μM under cytosolic/nuclear conditions. *J Inorg Biochem* 100:1800–1810. doi:10.1016/j.jinorgbio.2006.06.016

Yant SR, Mulato A, Hansen D, Tse WC, Niedziela-Majka A, Zhang JR, Stepan GJ, Jin D, Wong MH, Perreira JM, Singer E, Papalia GA, Hu EY, Zheng J, Lu B, Schroeder SD, Chou K, Ahmadyar S, Liclican A, Yu H, Novikov N, Paoli E, Gonik D, Ram RR, Hung M, McDougall WM, Brass AL, Sundquist WI, Cihlar T, Link JO. 2019. A highly potent long-acting small-molecule HIV-1 capsid inhibitor with efficacy in a humanized mouse model. *Nature Medicine* 25. doi:10.1038/s41591-019-0560-x

Zila V, Margiotta E, Turoňová B, Müller TG, Zimmerli CE, Mattei S, Allegretti M, Börner K, Rada J, Müller B, Lusic M, Kräusslich H-G, Beck M. 2021. Cone-shaped HIV-1 capsids are transported through intact nuclear pores. *Cell*. doi:10.1016/j.cell.2021.01.025

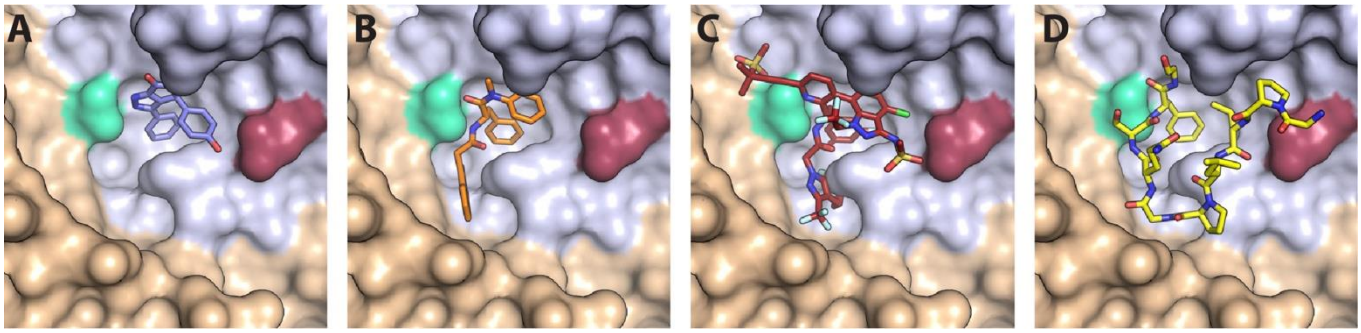

Figure 1. CA hexamer structures in complex with FG-binding pocket ligands. Two neighbouring CA molecules (grey, light brown) are shown as surface representation. Landmark residues N57 (pale green) and N74 (red-brown) are highlighted. Ligands are shown as sticks: **A.** BI-2. **B.** PF74. **C.** LEN. **D.** CPSF6 peptide. PDB IDs in A, B and D: 4U0F, 4U0E, 4U0A (Price et al., 2014). PDB ID in C: 6V2F (Link et al., 2020). Images were generated with PyMol version 2.3.5.

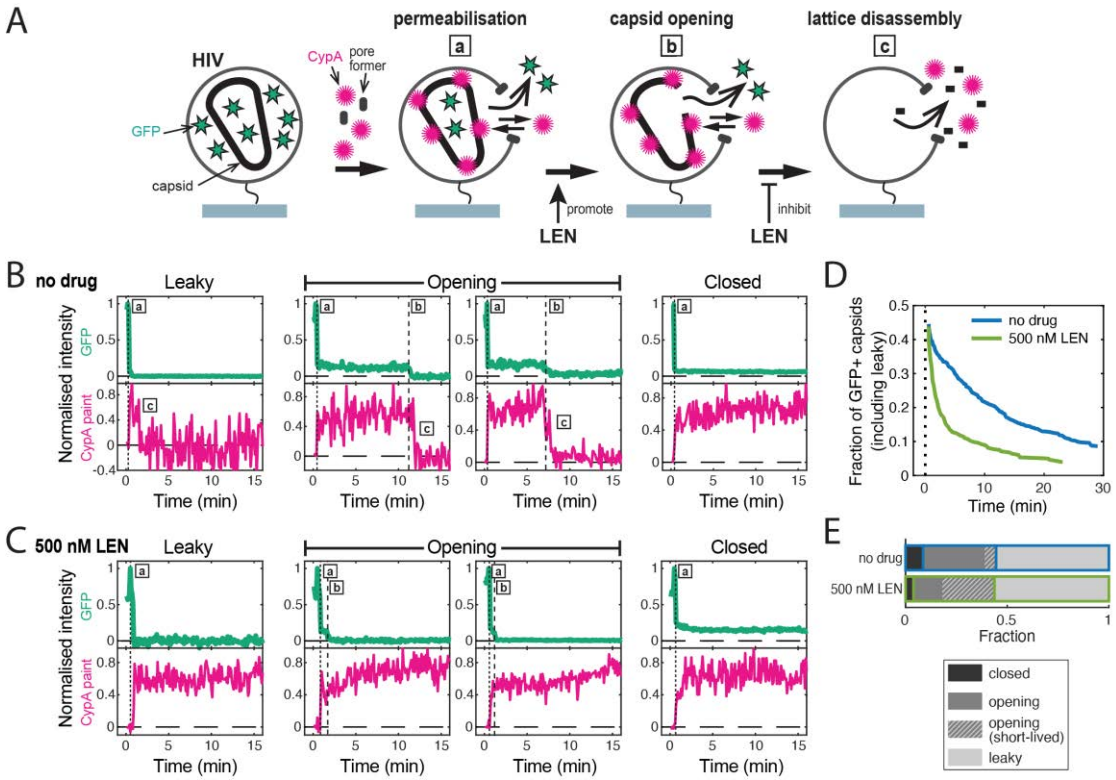

Figure 2. Single-particle HIV capsid uncoating kinetics measured by TIRF microscopy. A. Schematic diagram of a viral particle at different stages of uncoating detected in the assay. HIV particles were produced using a proviral construct with internal GFP that is released from the viral Gag protein during maturation and packaged as a solution phase marker inside the two compartments bound by the viral membrane and the capsid, respectively. These GFP-loaded HIV particles are immobilised on the coverslip surface and permeabilised in the presence of AF568-labelled CypA while recording fluorescence traces at the locations of individual HIV particles by TIRF microscopy. Permeabilisation of the viral membrane (step a) with a pore-forming protein leads to loss of ~80-90% of the GFP signal corresponding to the pool of GFP outside the capsid. AF568-CypA molecules diffuse through the membrane pores and bind to the capsid to reach a level that is proportional to the number of CA subunits in the capsid. Capsid opening (step b) leads to loss of the residual GFP that is inside the capsid. CA lattice disassembly (step c) is apparent from the rapid loss of the CypA paint signal. **B/C.** Example GFP release (blue-green) and CypA paint (magenta) traces for particles with capsids that are already leaky (i.e. contain defects and release all GFP in one step), undergo opening at various times after permeabilization or remain closed throughout the observation period. In the absence of drug (B), the CypA paint intensity decays rapidly when the capsid is no longer closed (complete loss of GFP signal). In the presence of 500 nM LEN (C), the CypA paint signal remains constant even when the GFP signal is completely lost showing that the drug stabilises the ruptured capsid. **D/E.** Analysis of all single-particle traces in the field of view to yield capsid survival curves (D) and fraction of leaky, opening and closed capsids at the end of the experiment (E) showing that LEN induces rupture of the capsid.

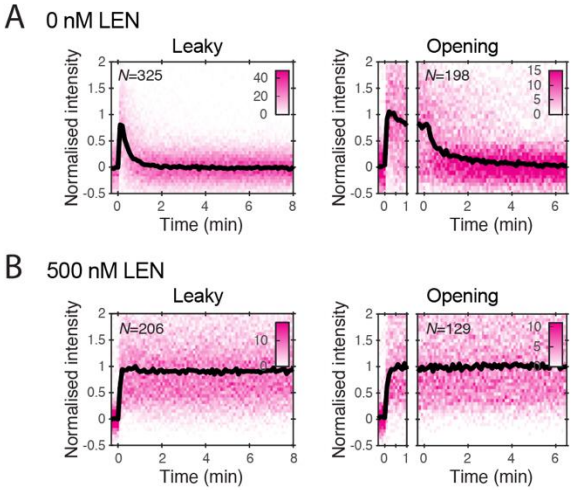

Figure 2–Figure Supplement 1. Heatmaps (magenta) and median traces (black line) of the CypA intensity measured at particles with leaky (left) or opening (right) capsids in the absence (A) or presence (B) of 500 nM LEN. LEN prevents dissociation of CA from the lattice of capsids that are no longer closed cones.

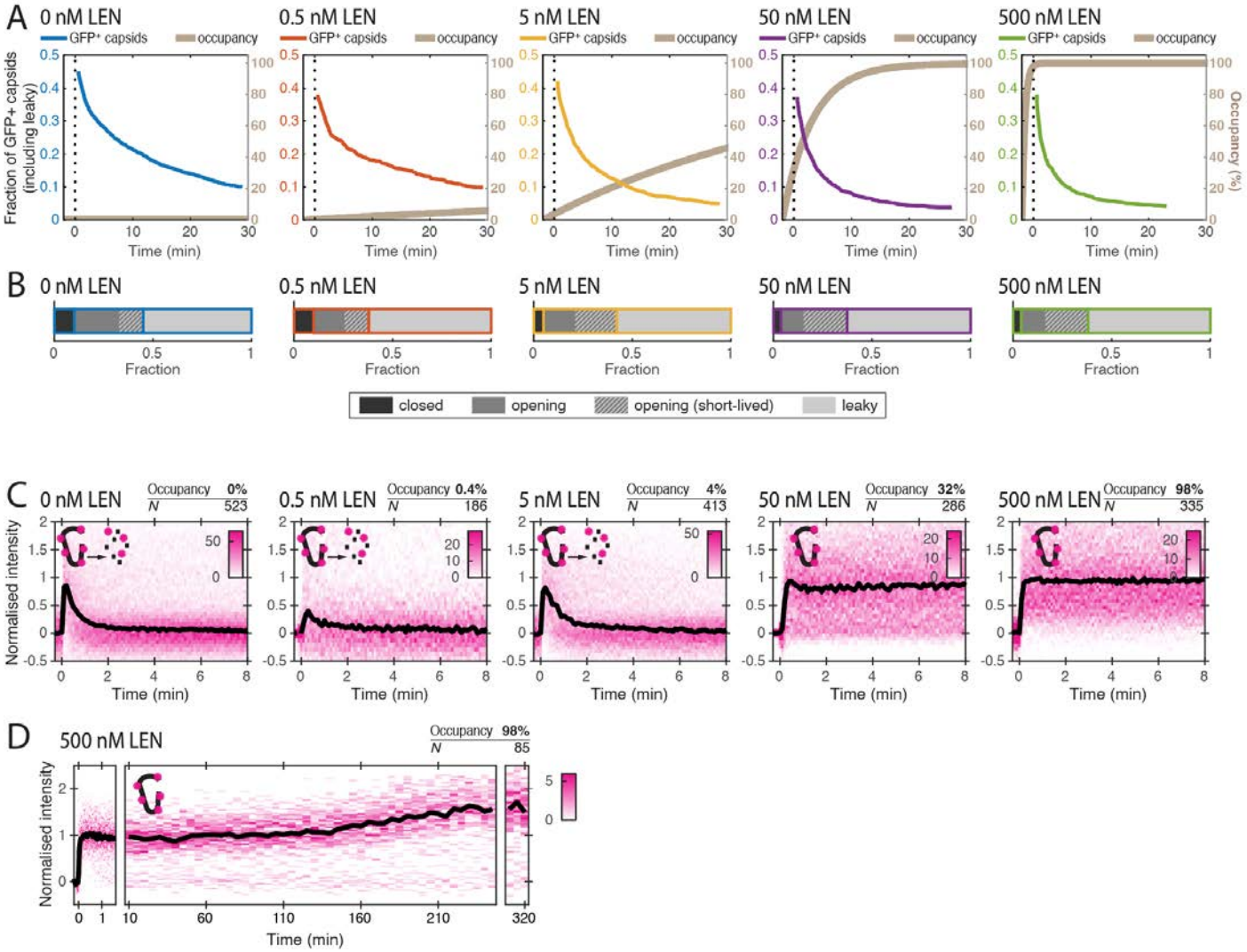

Figure 3. LEN accelerates capsid opening and subsequently promotes CA lattice stability. Single-particle analysis of the effect of 0–500 nM LEN on capsid uncoating via GFP release and CypA paint. **A/B.** Capsid survival curves (A) and fraction of leaky, opening and closed capsids at the end of the experiment (B) showing that the drug induces rupture of the capsid. Pooled data from multiple experiments (total number of traces): 0 nM (4325); 0.5 nM (1242); 5 nM (1585); 50 nM (1520); 500 nM (1048). **C.** Heatmaps (magenta) and median traces (black line) of the CypA intensity measured at particles with leaky or opening capsids in the presence of 0–500 nM LEN showing that LEN stabilises the CA lattice of ruptured capsids above an occupancy threshold of ~30%. **D.** Heatmap (magenta) and median trace (black line) of the CypA intensity of particles (leaky/opening) showing that 500 nM LEN prevents CA loss from the ruptured capsid for at least 5 hours.

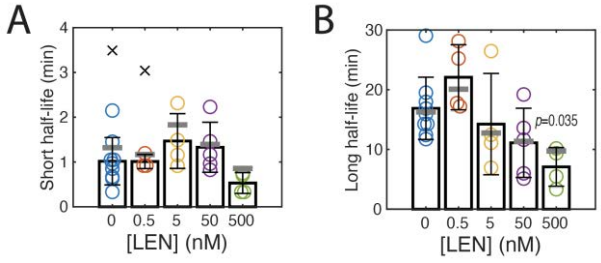

Figure 3–Figure Supplement 1. Half-lifes of the short-lived fraction (A) and the long-lived fraction (B) of opening capsids determined from a biexponential fit of survival curves. Each symbol represents an independent single-particle TIRF uncoating experiment. Outliers are indicated by the symbol '×'. Black bars represent the mean and error bars represent the standard deviation. The grey lines indicate the half-lives obtained from the fits of the survival curves of pooled data from all experiments at each concentration. Statistical comparison using one-way ANOVA with Dunnett's multiple comparison test. The differences between conditions are not statistically significant apart from the comparison between the long half-lives for control (0 nM LEN) and 500 nM LEN in panel B (p=0.035).

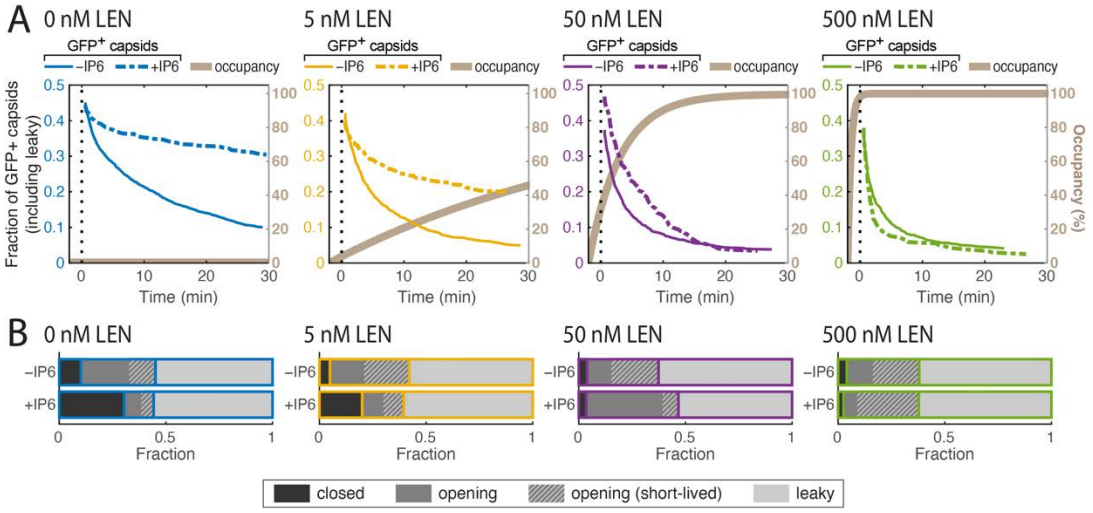

Figure 4. IP6 partially counteracts LEN-induced capsid rupture. Single-particle analysis of the effect of 0–500 nM LEN on capsid uncoating via GFP release and CypA paint in the presence of 100 µM IP6. The corresponding uncoating data in the absence of IP6 from Figure 3 is reproduced to facilitate comparison. **A/B.** Capsid survival curves (A) and fraction of leaky, opening and closed capsids at the end of the experiment (B) showing that IP6 partially counteracts the drug-induced rupture of the capsid at low but not high concentrations of LEN. Pooled data from multiple experiments (total number of traces): 0 nM LEN+IP6 (836); 5 nM LEN+IP6 (589); 50 nM LEN+IP6 (321); 500 nM LEN+IP6 (238).

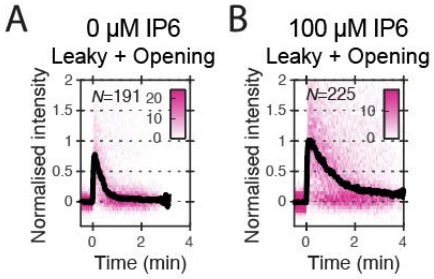

Figure 4–Figure Supplement 1. Heatmaps (magenta) and median traces (black line) of the CypA intensity measured at particles with leaky or opening capsids in the absence (A) or presence (B) of 100 µM IP6.

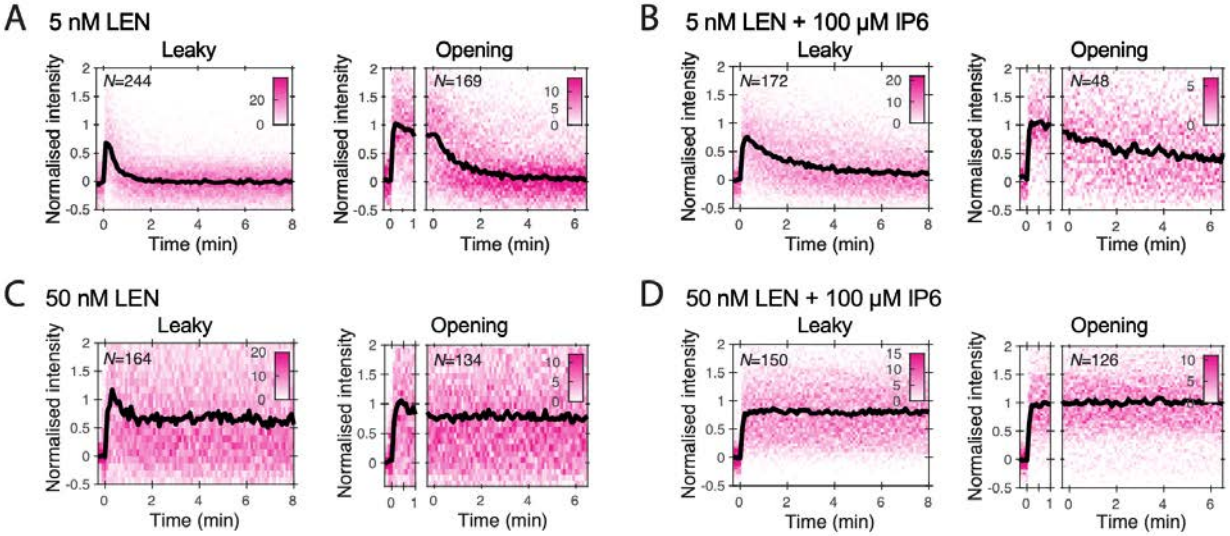

Figure 4–Figure Supplement 2. Heatmaps (magenta) and median traces (black line) of the CypA intensity measured at particles with leaky (left) or opening (right) capsids. **A/B.** 5 nM LEN in the absence (A) or presence (B) of 100 µM IP6. The presence of IP6 slows capsid disassembly in the presence of 5 nM LEN but does not prevent it. **C/D.** 50 nM LEN in the absence (C) or presence (D) of 100 µM IP6. 50 nM LEN stabilises the CypA paint signal, regardless of whether IP6 is present.

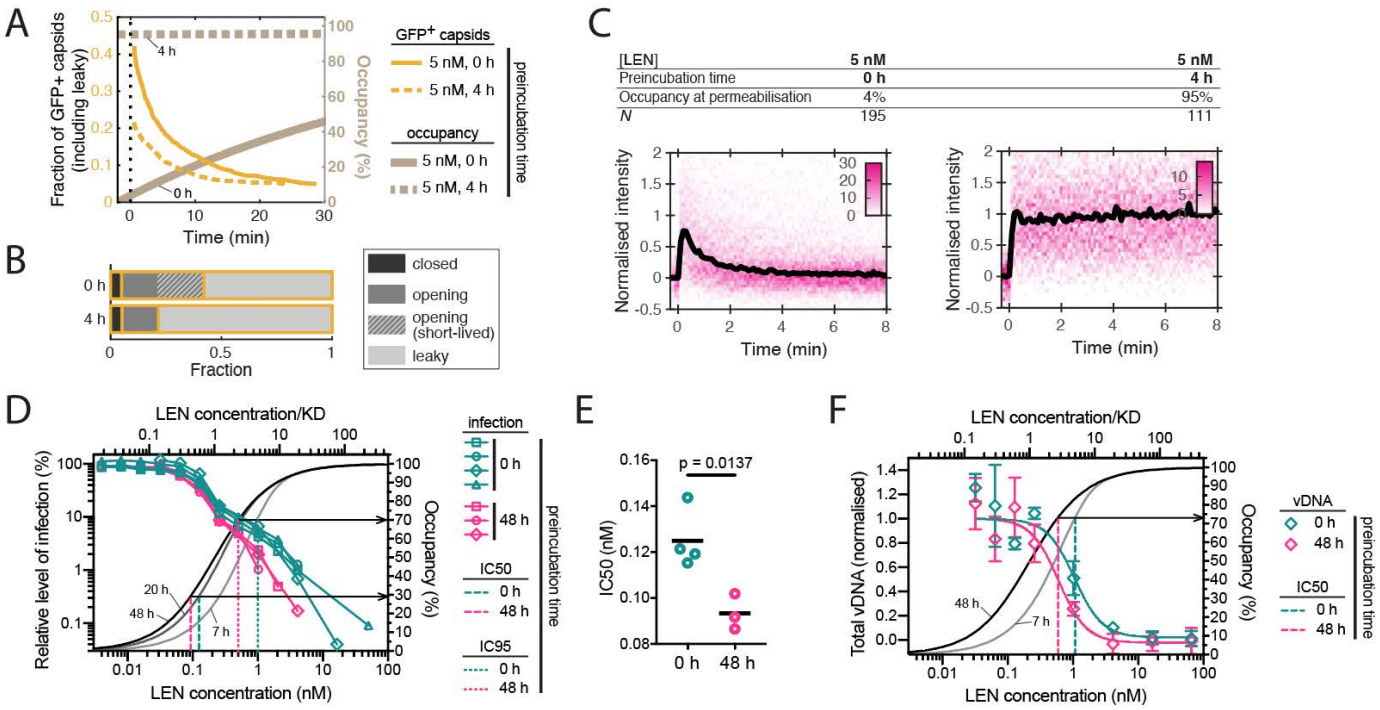

Figure 5. Preincubating HIV particles with LEN is required to obtain the full effect of the drug on capsid stability, HIV infection and reverse transcription. A-C. Single-particle analysis of capsid uncoating in the presence of 5 nM LEN added to the viral particles at the start (0 h preincubation) or 4 h before the start (4 h preincubation) of the TIRF assay. Capsid survival curves (A) and fraction of leaky, opening and closed capsids at the end of the experiment (B) show that preincubation with drug increases capsid rupture. Pooled data from multiple experiments (total number of traces): 5 nM LEN, 0 h (1585); 5 nM LEN, 4 h (1159). (C) CypA paint heatmaps and median CypA paint intensity traces of leaky and opening capsids show that preincubation is required to stabilise the CA lattice after capsid rupture. **D.** Dose-response curves of Jurkat cells infected with VSV-G-pseudotyped GFP-encoding virus that was preincubated for 0 h or 48 h with the corresponding concentration of LEN. The number of infected cells was determined by flow cytometry 48 h post infection. Data points represent percent infectivity relative to the vehicle control. The graph shows data from four (0 h preincubation) or three (48 h preincubation) independent experiments. The vertical dashed lines indicate the IC50 values determined from least squares fits of the curves and the vertical dotted lines indicate the IC95 values determined as the concentration where the relative level of infection reaches 5% (0 h preincubation: 1.024 nM [5.3% infection]; 48 h preincubation: 0.512 nM [5.1% infection]). **E.** Relative IC50 values determined from least squares fits of the data in D giving values of 125±13 pM without preincubation and 93±8 pM with 48 h preincubation. Statistical analysis using an unpaired two-tailed t-test. **F.** Quantification using qPCR of total viral DNA from Jurkat cells collected 24 h after infection with VSV-G-pseudotyped GFP-encoding virus as in panel D (with 0 h or 48 h preincubation with LEN). Normalized copy numbers (mean ± SD) from two independent experiments with two technical repeats each. Least squares fit (solid line) providing IC50 values of ~1080 pM without preincubation and ~590 pM with 48 h preincubation.

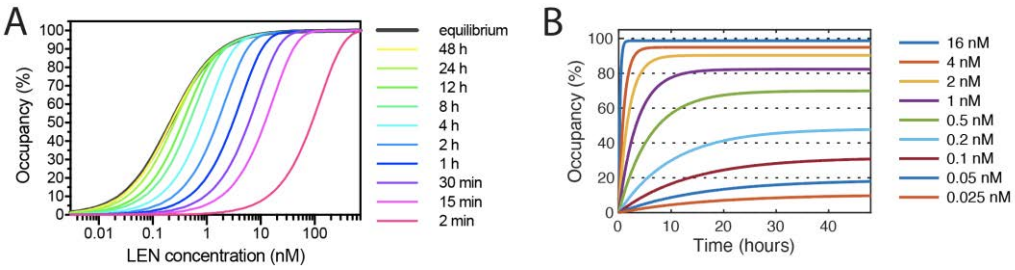

Figure 5–Figure Supplement 1. Occupancy of binding pockets on the CA lattice with LEN as a function of concentration (A, plotted for different time points) and as a function of time (B, plotted for different concentrations). Curves were calculated using k_{on} = 6.5E4 $M^{-1}s^{-1}$ and k_{off} = 1.4E-5 s^{-1} determined by surface plasmon resonance spectroscopy (Link et al., 2020).

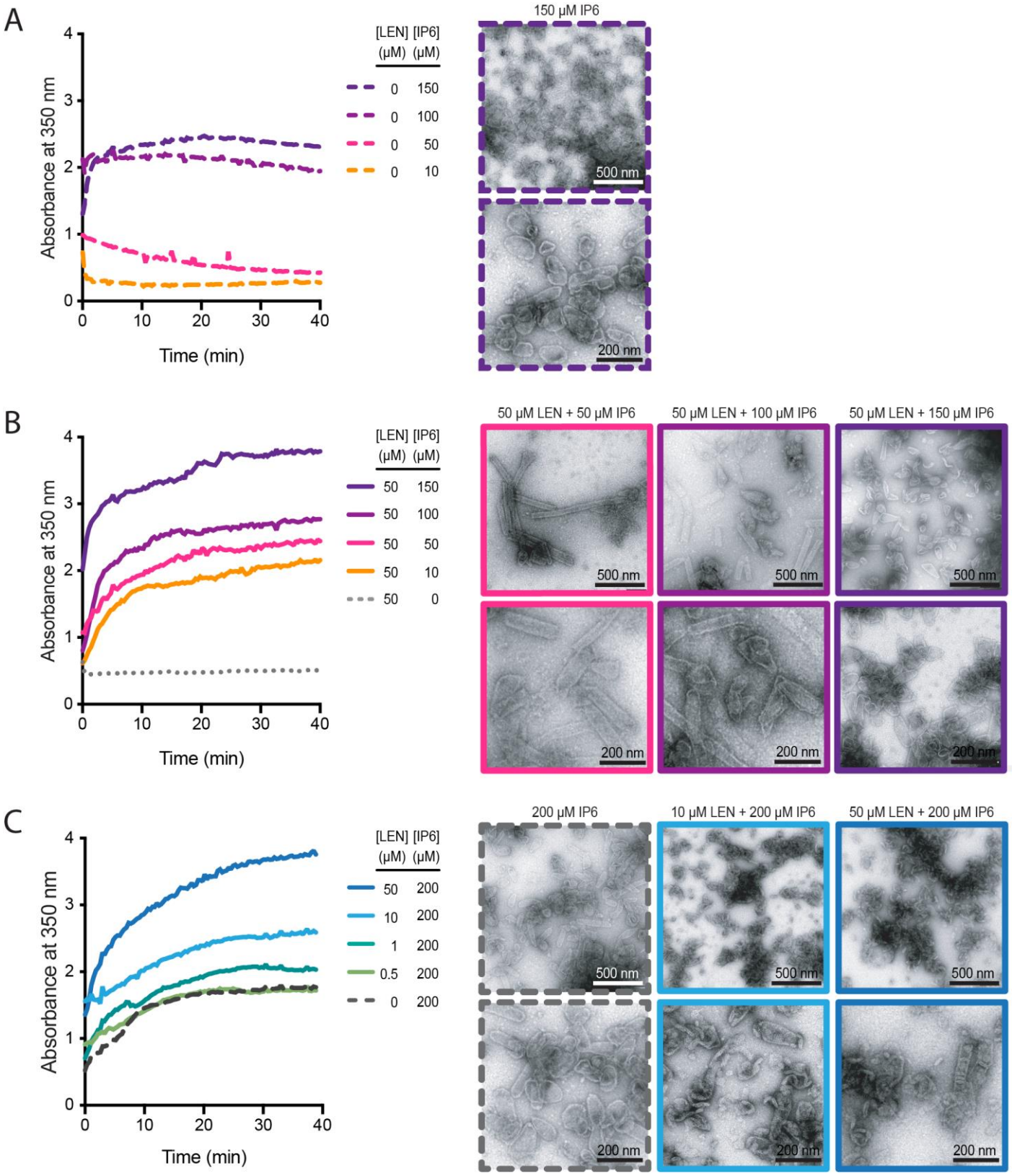

Figure 6. IP6 and LEN synergise to promote CA assembly. In vitro assembly reactions of CA (75 μM) were carried out in 50 mM MES (pH 6.0) containing 1 mM DTT and monitored in real time by absorbance measurements at 350 nm. The assembly products obtained at the end of the reaction were imaged by negative staining electron microscopy. **A/B.** Assembly kinetics (left) and products (right) formed at 10–150 μM in the absence (A) or the presence (B) of 50 μM LEN. **C.** Assembly kinetics (left) and products (right) formed at 0–50 μM LEN in the presence of 200 μM IP6.

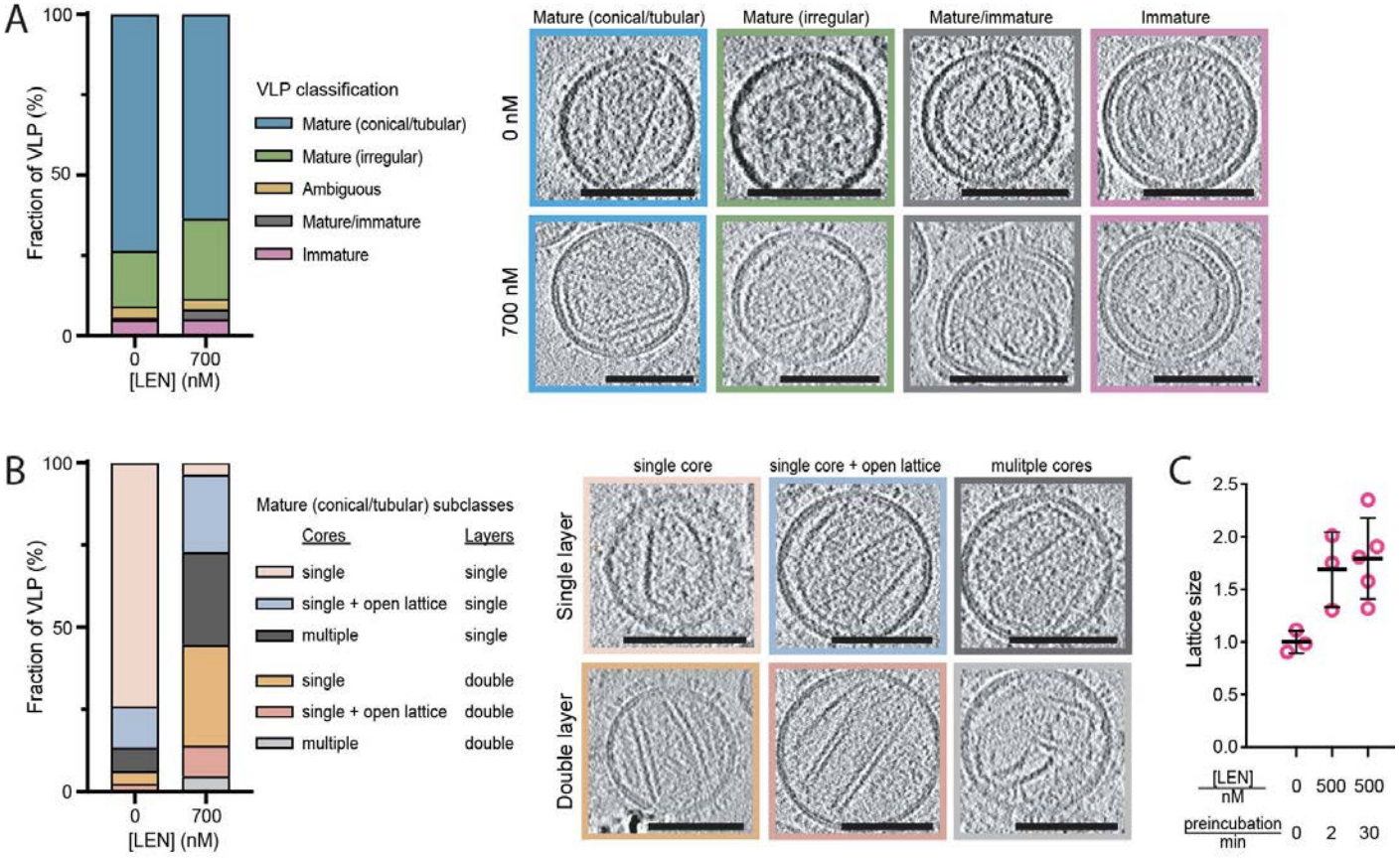

Figure 7. LEN promotes assembly of additional CA structures outside the capsid in mature HIV particles. A/B. CryoET analysis of untreated HIV and HIV incubated with 700 nM LEN for 30 min. A total of 139 untreated and 96 drug-treated viral particles were analysed, and the frequency of each phenotype is plotted as a percentage in the bar plots. Slices through representative tomograms of each phenotype are shown. Scale bars, 100 nm. (A) Virions were classified as either immature, mature/immature, ambiguous, mature (irregular) or mature (conical/tubular). (B) The mature (conical/tubular) particles from C were further divided into subclasses reflecting the number of CA assemblies and the absence or presence of assemblies with two CA layers. **C.** CypA paint intensity analysis to estimate the level of CA lattice assembly ("lattice size") in HIV particles preincubated with 500 nM LEN for 30 min before permeabilization relative to the lattice size of closed capsids in untreated HIV particles. Comparison of lattice size in untreated control (3 experiments) and HIV preincubated with 500 nM LEN for 2 minutes (3 experiments) or 30 minutes (4 experiments) showing that drug induces an increase in lattice size. An example CypA paint heatmaps is shown in Figure 7–Figure Supplement 1.

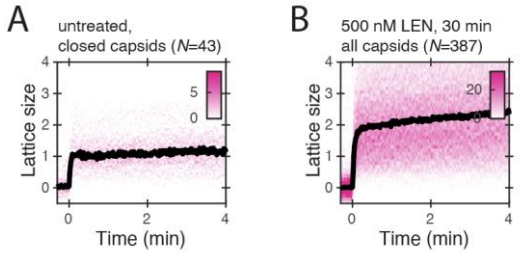

Figure 7–Figure Supplement 1. CypA paint intensity analysis to estimate the level of CA lattice assembly ("lattice size") in HIV particles preincubated with 500 nM LEN for 30 min before permeabilization relative to the lattice size of closed capsids in untreated HIV particles. Example CypA paint heatmaps (magenta) and median traces (black) of closed capsids in untreated HIV (A) and all capsids in HIV preincubated with drug (B).

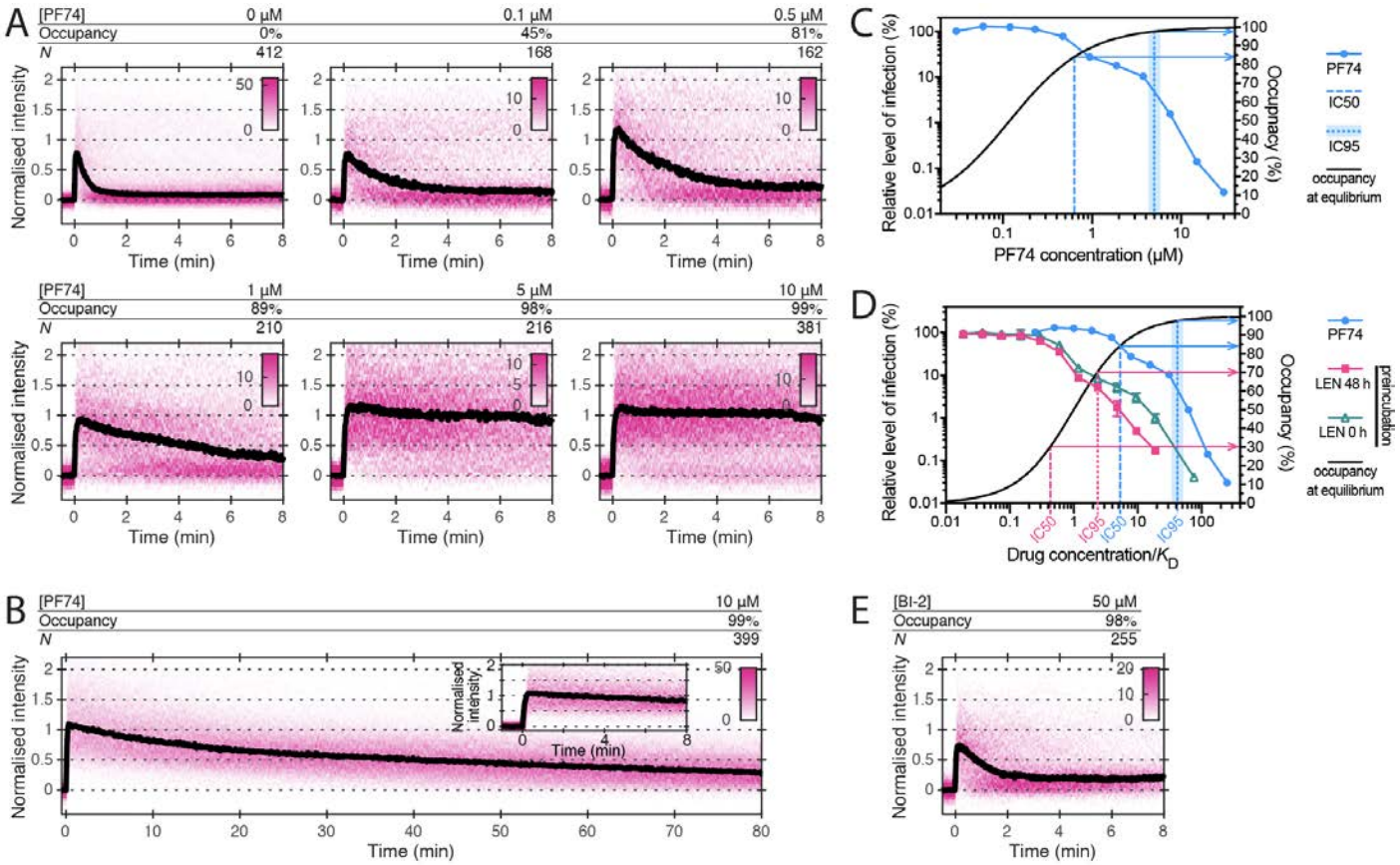

Figure 8. Effects of PF74 and BI-2 on CA lattice stability. A/B. Heatmaps (magenta) and median traces (black line) of the CypA intensity measured at particles with leaky or opening capsids in the presence of 0–10 µM PF74 showing that PF74 stabilises the CA lattice at concentrations >10-fold above the K_D of the drug-CA hexamer interaction. (A) PF74 titration in 8 min experiments. (B) 10 µM PF74 in an 80 min experiment showing that capsids disassemble over this time period. The inset shows the first 8 min of the trace. **C.** Dose-response curve of Jurkat cells infected with VSV-G-pseudotyped GFP-encoding virus in the presence of the indicated concentrations of PF74. The number of infected cells was determined by flow cytometry 48 h post infection. Data points represent percent infectivity relative to the vehicle control. The dotted lines indicate the IC50 determined from least squares fits of the curves (~0.6 µM, corresponding to ~5×K_D). **D.** Dose-response curves with drug concentration normalized by the K_D of the respective drug binding to CA hexamers for LEN (0 h and 48 h preincubation) and PF74 (same data as in Figure 5D and 8C, respectively). The dashed lines indicate the relative IC50 determined from least squares fits of the curves (~0.4×K_D for LEN [48 h preincubation] and ~5×K_D for PF74). **E.** Heatmap (magenta) and median trace (black line) of the CypA intensity at particles with leaky or opening capsids in the presence of 50 µM BI-2 showing that BI-2 does not stabilise the CA lattice.

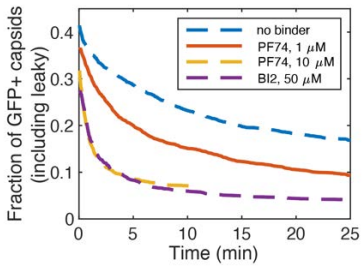

Figure 8 – Figure Supplement 1. PF74 and BI-2 binding at high occupancy leads to capsid rupture. Capsid survival curves were determined from GFP release traces. The control curve (no binder) and the curves determined in the presence of 10 uM PF74 and 50 uM BI-2 are reproduced from Marquez et al, 2018.

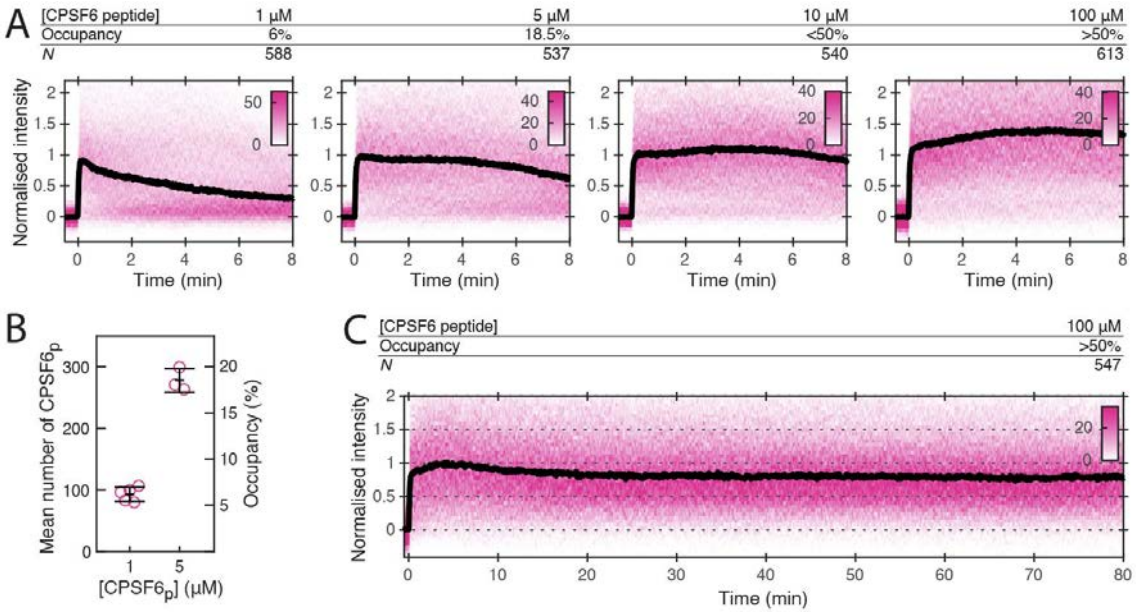

Figure 9. CPSF6 peptide stabilises the CA lattice at low occupancy. A. Heatmaps (magenta) and median traces (black line) of the CypA intensity measured at particles with leaky capsids in the presence of 1–100 µM CPSF6 peptide showing that the peptide stabilises the CA lattice at concentrations below the K_D of the peptide-CA hexamer interaction. **B.** Mean number of CPSF6 peptides bounds per capsid determined from CPSF6p-Cys-AF568 binding experiments. Each symbol represents an independent binding experiment, black bars indicate mean and standard deviation. **C.** Heatmap (magenta) and median trace (black line) of the CypA intensity at particles with leaky or opening capsids in the presence of 100 µM CPSF6 monitored over 80 minutes, showing long-term stabilisation of the CA lattice.

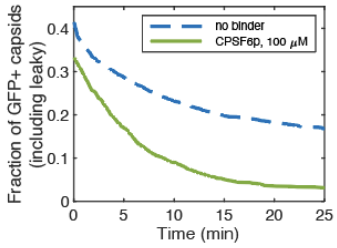

Figure 9 – Figure Supplement 1. Capsid survival curves were determined from GFP release traces. The control curve (no binder) is reproduced from Marquez et al, 2018.

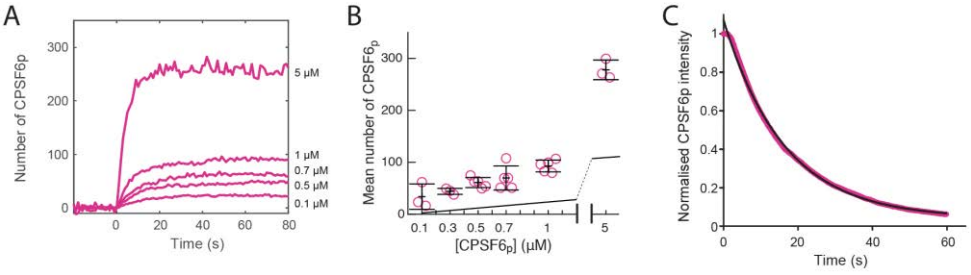

Figure 9 – Figure Supplement 2. Binding of CPSF6 peptide to closed capsids. A. Mean binding traces recorded at the indicated concentrations of labelled CPSF6 peptide. Binding traces were recorded at the locations of viral particles with closed capsid, whereby t = 0 corresponds to the time of viral membrane permeabilization. **B.** Mean number of labelled CPSF6 peptides bounds per capsid determined from binding experiments (see panel A for an example). Each symbol represents an independent binding experiment, black bars indicate mean and standard deviation. The black line represent the binding curve calculated using the published value of K_D=50 uM. **C.** Mean CPSF6 peptide intensity measured at closed capsids after wash-out of CPSF6 peptide from the flow channel at t = 0. The black line represents a fit of the data with a single exponential decay function.